Geothermics

CO2 and steam emissions by enhanced fracture permeability in the Monterotondo Marittimo-Sasso Pisano transfer fault system (Larderello Geothermal Field, Italy)

--Manuscript Draft--

Manuscript Number:	
Article Type:	Full Length Article
Section/Category:	Exploration technology
Keywords:	Fault zone permeability - CO2 flux - Steam emission - Larderello geothermal system - Discrete Fracture Network (DFN) - Geothermal exploration
Corresponding Author:	Marco Taussi, Ph.D. Universita degli Studi di Urbino Carlo Bo Dipartimento di Scienze Pure e Applicate Urbino, Marche ITALY
First Author:	Marco Taussi
Order of Authors:	Marco Taussi
	Andrea Brogi
	Domenico Liotta
	Barbara Nisi
	Maddalena Perrini
	Orlando Vaselli
	Miller Zambrano
	Martina Zucchi
Abstract:	Carbon dioxide is one of the most important gases naturally released from geothermal systems. Establishing the processes and pathways that regulate the CO2 diffuse degassing can provide valuable information for exploration and exploitation purposes of geothermal reservoirs. Areas with high CO2 emissions are indeed able to reveal major upflow zones from deep reservoirs through deep-reaching permeable fault zones. In this work, a high-resolution CO2 flux (with records up to 2927 g m-2 d-1) and soil temperature (with records up to 98.8 °C) survey was carried out along with detailed fracture parameters measurements in a selected area of the Monterotondo Marittimo-Sasso Pisano transfer fault (Larderello geothermal system, Tuscany, Italy). The main aim is to define the behavior of diffuse CO2 through the fault system and investigate how the soil CO2 flux and steam change with respect to the architecture of the fault damage zone (i.e., volumetric fracture intensity, permeability, and persistence of the fractures). The presence of multiple populations of CO2 flux suggested that three different transport mechanisms controlled soil degassing: i) purely diffusive, ii) mixed diffusive-advective, and iii) purely advective, characterized by efflux values of <20, between 20 and 300 and >300 g m-2 d-1, respectively. The spatial distribution of these fluxes well agrees with the fracture distribution and characters of the Jurassic radiolarite (Diaspri Fm) dissected by NNE-striking faults. The interaction between pre-existing fractures and fracture-related fault-zone locally enhances the secondary rock permeability as highlighted by the correlation between Discrete Fracture Network (DFN) modeling and advective flux. Eventually, by normalizing the CO2 output to the fault strip (1350 m2), a release of CO2 equal to ~155 t d-1 km-2 was estimated, although when the area characterized by advective flux (460 m2) was considered the efflux rose to 326 t d-1 km-2, confirming the pivotal role of fault zones in controlling fluid emissions.
Suggested Reviewers:	Giovanni Chiodini Director of Research, INGV: Istituto Nazionale di Geofisica e Vulcanologia giovanni.chiodini@ingv.it Great expertise in CO2 diffuse degassing and its link with geological structures
	Luca Smeraglia, PhD Researcher, IGAG CNR: Istituto di geologia ambientale e geoingegneria Consiglio

	Nazionale delle Ricerche luca.smeraglia@cnr.it Expertise on fault zones, fluid migration and DFN models
	Jerry P. Fairley, PhD Professor, University of Idaho jfairley@uidaho.edu Great expertise in geothermal fluids circulation through faults and fractures

1506
UNIVERSITÀ DEGLI STUDI DI URBINO CARLO BO
DISPEA
DIPARTIMENTO DI SCIENZE PURE E APPLICATE

Dear Editor,

We are pleased to submit the manuscript entitled "**CO_2 and steam emissions by enhanced fracture permeability in the Monterotondo Marittimo-Sasso Pisano transfer fault system (Larderello Geothermal Field, Italy)**" by *Taussi M., Brogi A., Liotta D., Nisi B., Perrini M., Vaselli O., Zambrano M., Zucchi M.*, to be considered for possible publication in Geothermics.

This work presents and discusses the results derived from a high-resolution CO_2 flux and soil temperature survey (grid 3 x 3 m) along with detailed measurements of fracture parameters in a selected area (1350 m^2) located along the Monterotondo Marittimo-Sasso Pisano transfer fault, in the worldwide famous Larderello geothermal area (Tuscany, Italy). This fault zone was exploited for geothermal purposes during the past decades, as it plays as a preferential way for the ascent of deep-sourced fluids. Along the fault zone, widespread hydrothermal alteration processes, fumarolic and boiling-pool manifestations and soil diffuse degassing are located.

The main aim of our work was to describe the behavior of the geothermal emissions through the fault system at the outcrop scale and investigate how the CO_2 flux and steam are changing in relation to the architecture of the fault damage zone.

The integration between CO_2 flux measurements and fracture distribution, elaborated through Discrete Fracture Network models, allowed to recognize that fracture-induced permeability and volumetric fracture intensity are the main factors in controlling the release of CO_2 and steam, with small variations of the two parameters that influence the transport mechanisms of CO_2.

Diffusive transport was recognized where permeability and fracture density were lower, confining the gases to flow through the strata-bounds and permitting strong CO_2 isotopic fractionation and steam condensation. On the contrary, advective transport was documented in the fault shear zone, where pervasive faults and fractures enhanced the permeability and favored a rapid movement of the geothermal fluids toward the surface, resulting in high CO_2 (up to 2927 g m^{-2} d^{-1}) and heat (temperature up to 98.8 °C) emissions, coupled with low-to-absent CO_2 isotopic fractionation. A mixing of the two transport mechanisms was also found in those areas characterized by intermediate values of permeability, locally influenced by incipient faults.

Our work not only highlights that faults and fractures associated to transfer zones play a key role in conveying geothermal fluids at the surface, but also describe and measure their geometric parameters in relation to CO_2 and steam emissions.

This work has not been previously published in any form, it is not under consideration for publication elsewhere, and if accepted it will not be published elsewhere in the same form, or in any other language, without the written consent of the publisher.

On the behalf of the Authors,

Sincerely,
Marco Taussi

Dr. Marco Taussi
Via Ca' Le Suore, 2/4 - 61029 Urbino PU, Italy
Tel. +39 328 02 03 358
marco.taussi@uniurb.it

Highlights

CO_2 degassing and faults/fractures in the Monterotondo-Sasso Pisano transfer fault

CO_2 flux, temperature, volumetric fracture intensity and permeability survey

Discrete Fracture Network modeling to reconstruct the fault architecture

CO_2 flux and steam change in relation to the architecture of the fault damage zone

Increased degassing rates evidence enhanced structural permeability

CO_2 and steam emissions by enhanced fracture permeability in the Monterotondo Marittimo-Sasso Pisano transfer fault system (Larderello Geothermal Field, Italy)

Marco Taussi [1*], Andrea Brogi [2,3], Domenico Liotta [2,3], Barbara Nisi [4], Maddalena Perrini [2], Orlando Vaselli [4,5], Miller Zambrano [6], Martina Zucchi [2]

[1] *University of Urbino Carlo Bo, Department of Pure and Applied Sciences, Via Ca' Le Suore 2/4, Urbino, Italy.*
[2] *University of Bari Aldo Moro, Department of Earth and Geoenvironmental Sciences, Via E. Orabona 4, Bari, Italy.*
[3] *IGG-CNR, Institute of Geosciences and Earth Resources, Via G. Moruzzi 1 - Pisa, Italy.*
[4] *IGG-CNR, Institute of Geosciences and Earth Resources, Via G. La Pira 4, Firenze, Italy.*
[5] *University of Florence, Department of Earth Sciences, Via G. La Pira, 4, Firenze, Italy.*
[6] *University of Camerino, School of Science and Technology, Via Gentile III da Varano 27, Camerino, Italy*

* Corresponding author: marco.taussi@uniurb.it

Abstract

Carbon dioxide is one of the most important gases naturally released from geothermal systems. Establishing the processes and pathways that regulate the CO_2 diffuse degassing can provide valuable information for exploration and exploitation purposes of geothermal reservoirs. Areas with high CO_2 emissions are indeed able to reveal major upflow zones from deep reservoirs through deep-reaching permeable fault zones. In this work, a high-resolution CO_2 flux (with records up to 2927 g m^{-2} d^{-1}) and soil temperature (with records up to 98.8 °C) survey was carried out along with detailed fracture parameters measurements in a selected area of the Monterotondo Marittimo-Sasso Pisano transfer fault (Larderello geothermal system, Tuscany, Italy). The main aim is to define the behavior of diffuse CO_2 through the fault system and investigate how the soil CO_2 flux and steam change with respect to the architecture of the fault damage zone (i.e., volumetric fracture intensity, permeability, and persistence of the fractures). The presence of multiple populations of CO_2 flux suggested that three different transport mechanisms controlled soil degassing: i) purely diffusive, ii) mixed diffusive-advective, and iii) purely advective, characterized by efflux values of <20, between 20 and 300 and >300 g m^{-2} d^{-1}, respectively. The spatial distribution of these fluxes well agrees with the fracture distribution and characters of the Jurassic radiolarite (Diaspri Fm) dissected by NNE-striking faults. The interaction between pre-existing fractures and fracture-related fault-zone locally enhances the secondary rock permeability as highlighted by the correlation between Discrete Fracture Network (DFN) modeling and advective flux. Eventually, by normalizing the CO_2 output to the fault strip (1350 m^2), a release of CO_2 equal to ~155 t d^{-1} km^{-2} was estimated, although when the area characterized by advective flux (460 m^2) was considered the efflux rose to 326 t d^{-1} km^{-2}, confirming the pivotal role of fault zones in controlling fluid emissions.

Key words

Fault zone permeability – CO_2 flux – Steam emission – Larderello geothermal system – Discrete Fracture Network (DFN) – Geothermal exploration

1. Introduction

Carbon dioxide (CO_2) emissions naturally released from geothermal systems, and more generally from natural systems, are a timely theme object of scientific debates in the frame of natural vs. anthropogenic contribution of greenhouse gases, with the former being by far the most significant ones (e.g., Fischer and Aiuppa, 2020). However, while anthropogenic CO_2 emissions can be evaluated relatively easily, more difficult is the estimation of the amount of CO_2 naturally escaping from Earth's surface (Bertani and Thain, 2002). Different methodologies such as remote sensing (e.g., ground-based and air- and space-borne techniques; Queißer et al., 2019 and references therein) and in-situ (e.g., eddy covariance, accumulation chamber, and dynamic concentration methods, e.g., Parkinson, 1981; Chiodini et al., 1998; Camarda et al., 2006; Camarda et al., 2009; Lewicki and Hilley, 2009; Camarda et al., 2019) measurements are commonly adopted to determine the flux of CO_2 escaping from the ground.

In the last decades, CO_2 flux measurements were carried out from several geothermal sites worldwide such as Brady's (USA; Jolie et al., 2015, 2016), Ohaaki, Taupo, and Rotorua (New Zealand; Werner and Cardellini, 2006; Rissmann et al., 2012), Los Humeros (Mexico; Peiffer et al., 2018; Jentsch et al., 2020), Furnas (Azores; Viveiros et al., 2010; 2020), Copahue, Cerro Blanco, Cordón de Inacaliri and Cerro Pabellón (Argentina and Chile; Chiodini et al., 2015; Lamberti et al., 2019, 2021; Taussi et al., 2019, 2021), Yangbajain (Tibet; Chiodini et al., 1998), Reykjanes, Hengill and Krýsuvík (Iceland; Fridriksson et al., 2006; Hernandez et al., 2012; Gudjónsdóttir et al., 2020), Latera, Mount Amiata, Torre Alfina (Italy; Chiodini et al., 2007, 2020; Nisi et al., 2014; Carapezza et al., 2015; Sbrana et al., 2020), among the others.

Despite the increasing efforts to provide precise estimates of CO_2 diffusing from geothermal (and volcanic) areas a lot of work is to be done before achieving a realistic output of CO_2 from these sources. Moreover, CO_2 measurements allow computing, though partially, the total CO_2 output from geothermal sites, since even extensive surveys are not able to entirely cover the areas due to large territories to be explored, uneven grounds, and free gas discharges. In addition, CO_2 emissions are subject to temporary (seasonal or permanent) changes linked, for example, to the variation of (i) atmospheric parameters (e.g., Klusman et al., 2000; Lelli and Raco, 2018; Delsarte et al., 2021), (ii) hydrothermal or volcanic system dynamics (e.g., Pérez et al., 2012; Werner et al., 2016; Cardellini et al., 2017); (iii) geothermal power plants operations (e.g., Bertani and Thain, 2002; Frondini et al., 2009; Rissmann et al., 2012; Fridriksson et al., 2017; Manzella et al., 2018; Jentsch et al., 2021), and (iii) transient permeability (e.g. Camarda et al., 2009). Although these limitations, measurements of natural CO_2 degassing are facilitated when the structural setting is known. Fluid circulation at high-to-moderate temperature as well as CO_2 escape is generally controlled by structural conduits in fault damage zones (e.g., Sibson, 2000; Fairley and Hinds, 2004; Rowland and Sibson, 2004; Lewicki et al., 2005; Werner and Cardellini, 2006; Anderson and Fairley, 2008; Faulkner et al., 2010; Faulds et al., 2011; Jolie et al., 2016; Lamberti et al., 2019; Barcelona et al., 2020), where fracture spacing, attributes (e.g., orientation, length, height, aspect ratio, intensity, and aperture), and distribution can strongly enhance permeability (Caine et al., 1996; Caine and Forster, 1999; Billi et al.; 2003; Agosta

et al.; 2010; Cox et al., 2001; Zucchi et al., 2017). The complexity of the architecture of the fracture network can be encompassed by using Discrete Fracture Network (DFN) models, which consist of statistical-based, realistic three-dimensional (3D) representations of the natural fracture network (Lucia, 1999; Nelson, 2001, Kim et al.; 2004), which can be upscaled with fracture hydraulic properties (porosity and permeability) in continuous models. Thus, considering that CO_2 emissions are mainly concentrated along fault zones (Curewitz and Karson, 1997; Jolie et al., 2016; Taussi et al., 2019, 2021; Lamberti et al., 2019; Jentsch et al., 2020), their geometrical reconstruction can offer the best opportunity to study CO_2 emission pathways, secondary mechanisms (e.g., reduction-oxidation processes of C-bearing species), and outputs along key transects across the fault zone under study.

In this paper, we present and discuss the results of a high-resolution soil CO_2 flux measurements coupled with soil temperatures, combined with the measurements of fracture parameters and DFN modeling along a fault zone crossing the worldwide famous Larderello geothermal area in its peripheral zone (Monterotondo Marittimo-Sasso Pisano area, hereafter MMSP; Fig. 1), where CO_2 emissions are accompanied by noticeable steam escaping. This fault zone, at least 5 km long, is part of a km-scale NE-oriented brittle shear zone, interpreted as part of a regional transfer zone (Gola et al., 2017; Liotta and Brogi, 2020) developed in the framework of the Neogene-Quaternary extensional tectonics affecting the inner Northern Apennines (Carmignani et al., 1994; Liotta et al., 1998; Brogi et al., 2005; Barchi, 2010).

The main goals are to i) verify the behavior of the diffused CO_2 and steam through the fault system; ii) investigate how the diffuse CO_2 fluxes and steam change with respect to the volumetric fracture intensity, permeability, and persistence of the fractures and iii) compute the total CO_2 output of the study area, comparing it with other geothermal areas.

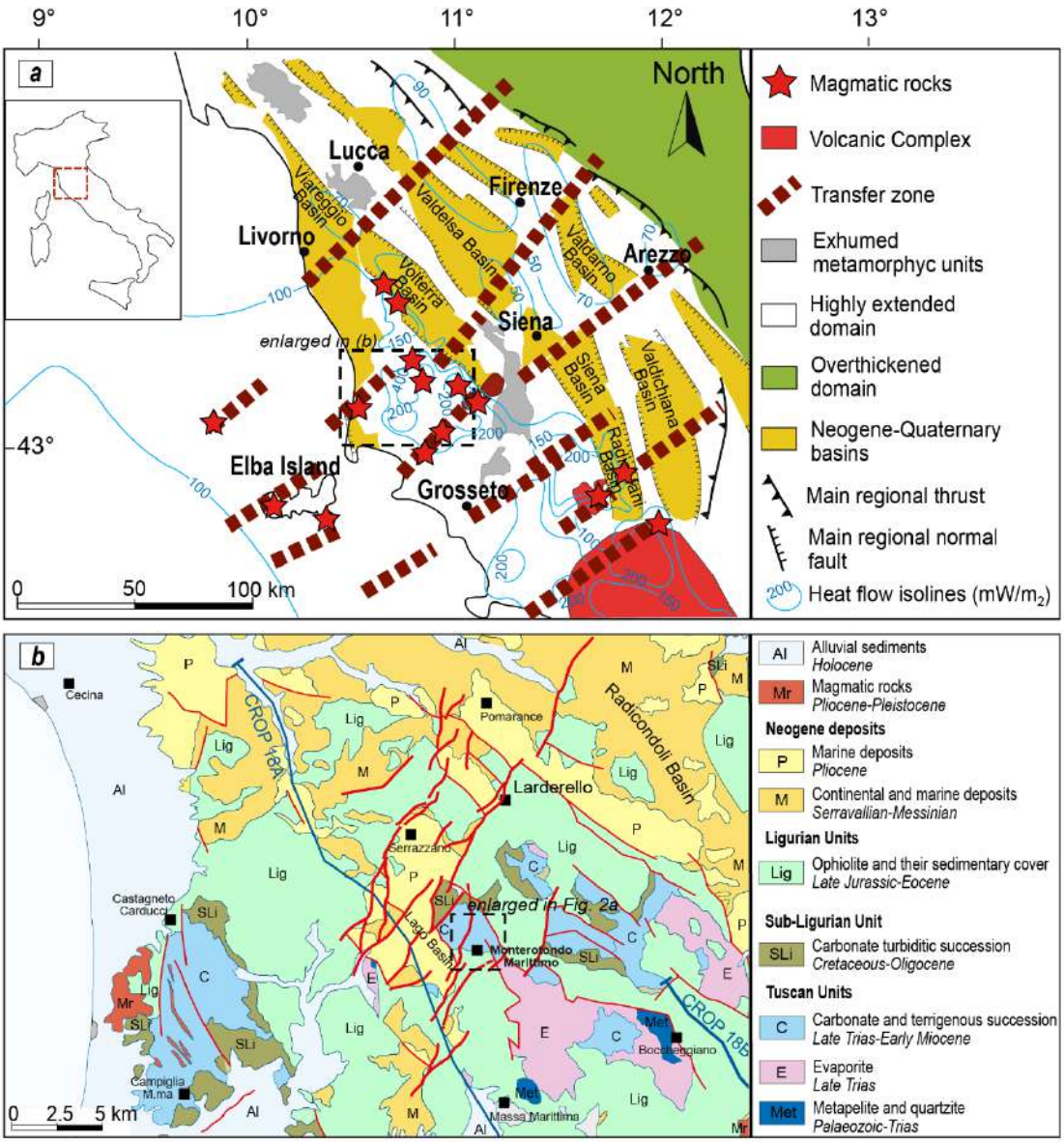

Figure 1. a) Structural sketch map of the Northern Apennines and Northern Tyrrhenian Sea; b) geological map of the Larderello area (modified after Liotta and Brogi, 2020). The study area is highlighted by the black dashed frame.

2. Geological background of the Larderello area

The Larderello geothermal area is a magmatic-driven geothermal system (Baldi et al., 1994; Bellani et al., 2004; Gola et al., 2017; Rochira et al., 2018) located in the inner Northern Apennines (Fig. 1a), a NE-verging Alpine belt (Vai and Martini, 2001) which experienced convergence and collisional processes (Cretaceous-early Miocene) and subsequent extension since early-middle Miocene (Carmignani et al., 1994). One of the clearest indications of the collisional process is given by high-pressure metamorphism (up to 1.5 GPa, Theye et al., 1997; Brunet et al., 2000; Rossetti et al., 2002; Bianco et al., 2019) developed during the eastward stacking of the tectonic units deriving from the oceanic (Ligurian units, *Auctt.*), transitional (Sub-Ligurian units, *Auctt.*) and continental (Tuscan Nappe, *Auctt.*) paleogeographic domains of Northern Apennines (Molli et al., 2008). The subsequent eastward migration of the extensional tectonics resulted in: (a) Miocene lateral segmentation of the previously stacked units (Brogi et al., 2005; Brogi and Liotta, 2008); (b) development of Pliocene-

Quaternary NW-striking normal faults cross-cutting all the previous structures and inducing NW-trending tectonic depressions, filled by continental and marine sediments (Martini and Sagri, 1993; Brogi, 2020; Martini et al., 2021). The primary evidence of extension is the opening of the Tyrrhenian Basin (Bartole, 1995) and the present crustal and lithospheric thickness of about 20 and 40 km, respectively (Calcagnile and Panza, 1980; Locardi and Nicolich, 1988; Di Stefano et al., 2011; Moeller et al., 2013). At least since the Langhian, extension was accompanied by eastward migrating magmatism (Serri et al., 1993), affecting the Tuscan archipelago and the inland inner Northern Apennines (Serri et al., 2001; Dini et al., 2005, 2008). Magmas were emplaced at shallow crustal levels (mainly at 6–8 km depth; Serri et al., 2001) mostly along the NE-striking brittle shear zones (Dini et al., 2008; Spiess et al., 2021 and references therein), which played the role of transfer zones in the inner Northern Apennines (Liotta, 1991; Dini et al., 2008) and lateral ramps in the outer Northern Apennines (Liotta, 1991), where coeval compression occurred (Elter et al., 1975). Currently, no active volcanoes are present in Tuscany although heat flux is 120 mW/m^2 on average (Della Vedova et al., 2001; Pauselli et al., 2019). However, local peaks up to 1000 mW/m^2 were estimated in the Larderello geothermal area (Baldi et al., 1994; Della Vedova et al., 2001), which is located along one of the most relevant transfer zones crossing the Northern Apennines (Fig. 1a) that hosts a Pliocene-Pleistocene pull-apart-like tectonic depression named Lago Basin (Fig. 1b). The latter developed where a cooling magma is localized at depth and geothermal fluid flow is particularly active (Gola et al., 2017; Rochira et al., 2018; Liotta and Brogi, 2020), contributing to determining the bulk of the electricity production of the Larderello geothermal field (Barbier, 2002; Romagnoli et al., 2010).

The tectonic and stratigraphic units occurring in the Larderello area have been described by several authors (e.g., Lazzarotto, 1967; Lazzarotto and Mazzanti, 1978; Costantini et al., 2002; Elter and Pandeli, 1990; Pandeli et al., 1991, 1994; Dini et al., 2005; Bertini et al., 2006; Brogi and Cerboneschi, 2007; Romagnoli et al., 2010). In the MMSP area (Fig. 2), the carbonate, siliceous and terrigenous successions of the Tuscan Nappe are broadly exposed, surrounded by the Ligurian and Subligurian Units.

Information from deeper structural levels derive from deep boreholes drilled during the geothermal exploration and exploitation (Bertini et al., 1991; 2006; Romagnoli et al., 2010), and interpretation of reflection seismic lines. They display the occurrence of a high-impedance seismic reflector, named as K-horizon (Batini et al., 1978; Cameli et al., 1993), ranging in depth between 3 and 7 km, and deciphered as an active shear zone, located at the top of the brittle-ductile transition (Cameli et al., 1993, 1998; Liotta and Ranalli, 1999; De Matteis et al., 2008), possibly hosting fluids in supercritical conditions (Agostinetti et al., 2017). The K-horizon shows a dome-shaped culmination West to the MMSP area, in correspondence with the Lago Basin (Liotta and Brogi, 2020 and references therein). Here, the highest values of heat flow (Baldi et al., 1994; Della Vedova et al., 2001), and relatively high ^{3}He/^{4}He isotopic ratios (Magro et al., 2003) were measured, suggesting that the Lago Basin is a preferential area for mantle-derived fluids escaping. The study area is in the shoulders of this basin, where the Neogene substratum crops out (Fig. 1b) and the natural CO_2 emissions are located.

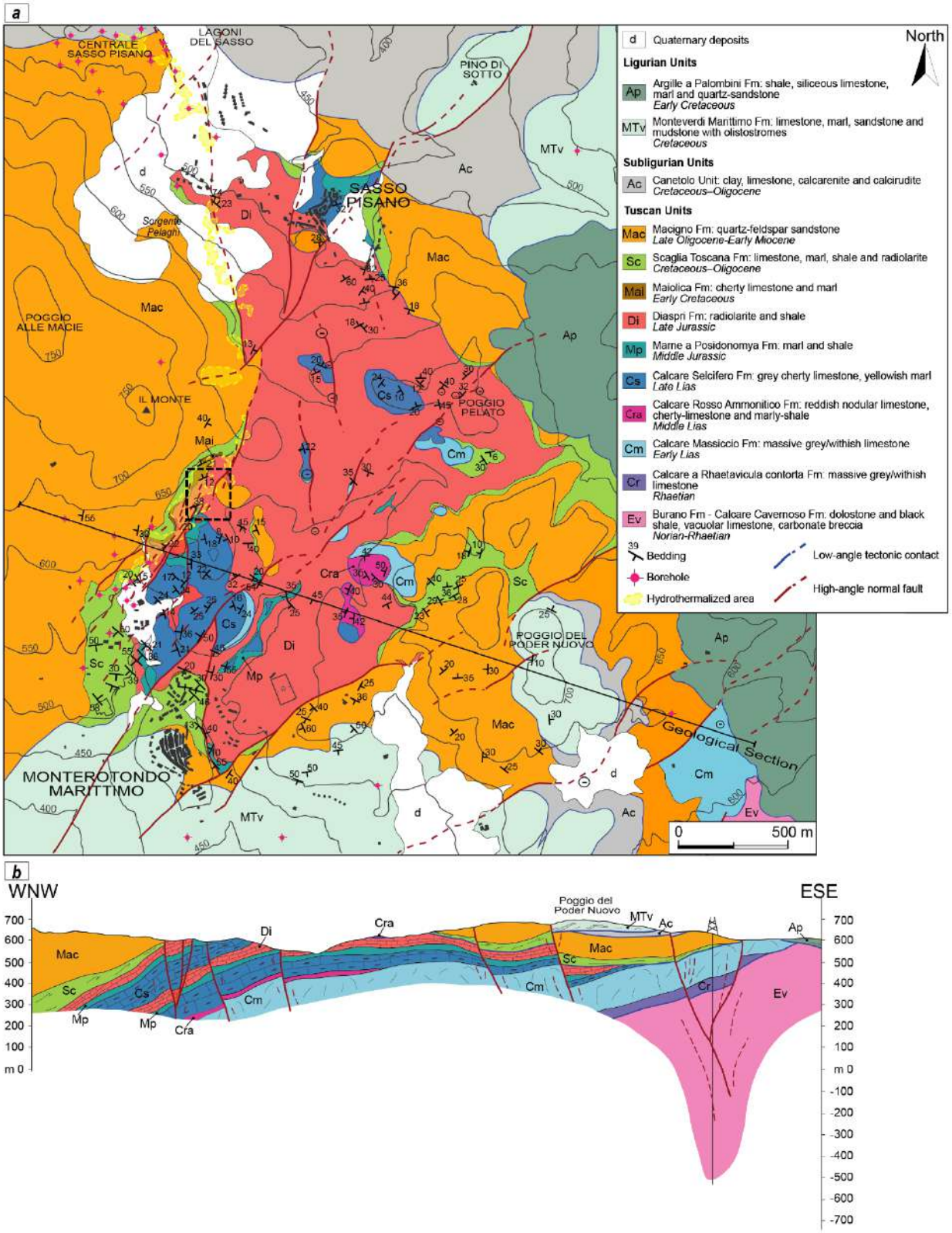

Figure 2. a) Geological and structural map of the Monterotondo Marittimo-Sasso Pisano (MMSP) area in which the main fault zone and the study area (black dashed frame) are highlighted; b) geological section across the study area. Its trace is indicated in (a).

3. Hydrothermal manifestations

"Le Biancane" natural park comprehends some of the numerous areas characterized by hydrothermalized surfaces that occur between Monterotondo Marittimo and Sasso Pisano villages

which extend from <1,000 up to >40,000 m^2 (Fig. 3). Alteration and kaolinization produced the typical bleaching process, which mainly involves the marly-clay and siliceous lithotypes, whereas Fe-oxides and hydroxides developed on the terrigenous succession of the Tuscan Domain (Orlandi, 2006; Bentivegna, 2010; Regione Toscana, 2014).

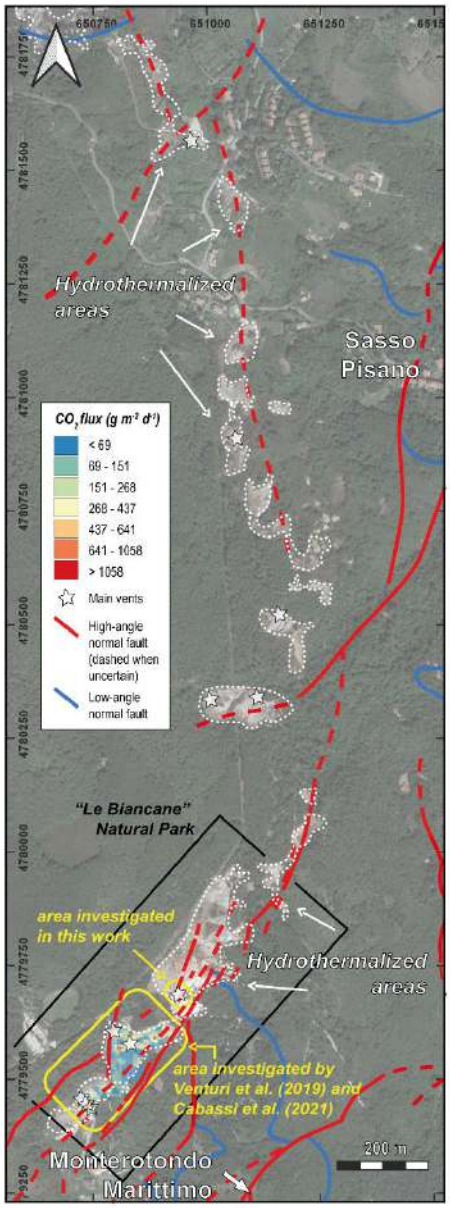

Figure 3. Hydrothermalized zones along the Monterotondo Marittimo-Sasso Pisano fault zone. The location of the main faults and hydrothermal vents (after Venturi et al., 2019; Leila et al., 2021; maga database www.magadb.net) are also reported and the diffuse soil CO_2 measurements by Venturi et al. (2019) and Cabassi et al. (2021) are highlighted.

Geothermal manifestations along the MMSP fault zone are represented by fumaroles, steam vents, acidic and boiling steam-heated pools, and mud pools called “lagoni” (e.g., Duchi et al., 1986, Minissale, 1991; Duchi et al., 1992) (Fig. 4). At the fumarole vents, acicular aggregates or encrustations of native sulfur are commonly found (Fig. 4), sometimes in association with gypsum, sulfates, and borates (Orlandi, 2006; Bentivegna, 2010).

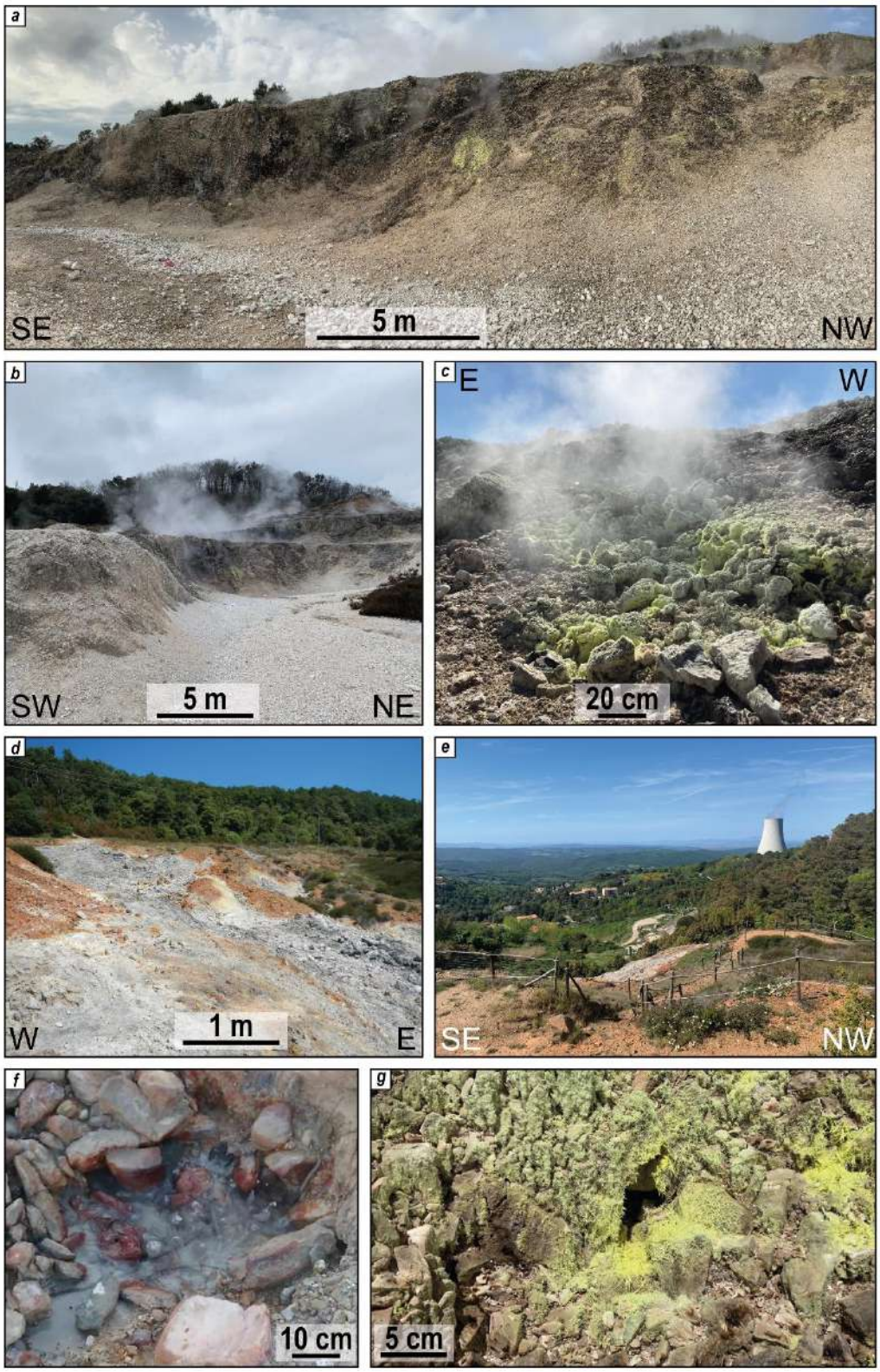

Figure 4. Field photographs from the "Le Biancane" natural park. a-b) wall of an abandoned quarry with visible fumaroles and steaming grounds; the rock scarp crosscuts the Monterotondo Marittimo-Sasso Pisano fault zone; c) fumarolic manifestations; d) hydrothermally altered grounds; e) panoramic view of the park with the geothermal power plant cooling tower in the background; f) bubbling pool; g) acicular aggregates and encrustations of native sulfur in a fumarolic vent.

The discharged fluids are mostly at the water boiling temperature and are dominated by H_2O (>95% v/v) followed by CO_2, N_2, H_2S, H_2, and CH_4, with minor amounts of O_2 and noble gases (Scandiffio

et al., 1995; Magro et al., 2003; Venturi et al., 2019; Leila et al., 2021). The fumarolic fluids at Sasso Pisano showed a $^{3}He/^{4}He$ (as R/Ra) up to 2.32 (Hooker et al., 1985) suggesting mixing processes, at variable degrees, between mantle (up to 40% when considering the MORB as representative of the mantle beneath Tuscany; Hooker et al., 1985) and crustal fluids (Magro et al., 2003). The R/Ra value of Sasso Pisano is higher than the one measured in the Lago fumaroles (i.e., 1.63; Minissale et al., 1997) but lower than the maximum value recorded in the geothermal wells (i.e., up to 3.2; Hooker et al., 1985). The isotopic composition of Carbon in CO_2 (expressed as $\delta^{13}C\text{-}CO_2$) of the Monterotondo Marittimo fumaroles range from −4.2 to −2.4‰ vs V-PDB (Venturi et al., 2019; Leila et al., 2021), and are similar to those recorded in the fluid discharges of Sasso Pisano (from −3.83‰ up to −2.3‰ vs V-PDB; Minissale et al., 1997; Tassi et al., 2012; Leila et al., 2021). These $\delta^{13}C\text{-}CO_2$ values are in the isotopic range observed for other fumaroles (e.g., from −7.26 to −0.26‰ vs V-PDB; Minissale et al., 1997) and geothermal wells (from −7.1 to −1.4‰ vs V-PDB; Gherardi et al., 2005) of the Larderello geothermal system. The isotopic data account for a CO_2 dual source (Gherardi et al., 2005), i.e. (i) magmatic degassing (i.e., −8 to −4‰ vs V-PDB; Mason et al., 2017) and (ii) decarbonation of carbonates and calc-silicates (i.e., −5 to +5‰ vs V-PDB; Venturi et al., 2017 and references therein).

Diffuse degassing of soil CO_2, $\delta^{13}C\text{-}CO_2$ in interstitial gas, soil temperatures and gaseous elemental mercury (GEM) emissions were measured in a selected area of about 20,000 m^2 within the “Le Biancane” natural park, located just 100 m SW from the study area (Fig. 3), by Venturi et al. (2019) and Cabassi et al. (2021) during the summer season. These authors measured CO_2 fluxes ranging from <2 up to 2,144 g m^{-2} d^{-1} linked to soil temperature from 27.1 to 94.5 °C, the latter also in agreement with those measured by Silvestri et al. (2020) through remote sensing. The soil CO_2 fluxes showed no spatial correlation with soil temperature, nor with GEM emissions, which were ranging from below the detection limit up to 0.65 µg m^{-2} d^{-1} (Cabassi et al., 2021). Noteworthy, these authors also evidenced the presence of microbiological activity in the hydrothermalized soils, suggesting that it plays an important role in both governing the, CO_2, CH_4 and GEM emission and affecting the $\delta^{13}C\text{-}CO_2$ composition of the interstitial gas, the latter showing a general enrichment in ^{13}C ($\delta^{13}C\text{-}CO_2$ up to +3.41‰ vs V-PDB) with respect to the carbon isotopic signature of the fumaroles.

4. Methods

To reconstruct the relationships among fractures and CO_2 flux and steam escaping from the soil, geochemical and geological surveys in selected areas of the “Le Biancane” natural park (Fig. 3) were carried out.

4.1 Soil CO_2 flux and temperature measurements

In July 2021, 75 soil temperature and CO_2 flux measurements were carried out with stable weather conditions and dry soils in the selected fault zone of the study area using the accumulation chamber method (e.g., Chiodini et al., 1998, Carapezza and Federico, 2000; Cardellini et al., 2003; Viveiros

et al., 2010, 2020; Nisi et al., 2013; Lamberti et al., 2019; Taussi et al., 2021). The survey was carried out following as much as possible a regular grid of about 3 x 3 m over a restricted area of 1350 m^2 (0.00135 km^2), where each node was located with a portable GPS Garmin GPSmap 62st. Next to each soil CO_2 sampling point, soil temperatures were measured using a TERSID thermocouple inserted into the soil for a couple of centimeters (dynamic range from −20 to 1150 °C; uncertainty ± 0.1 °C; Tassi et al., 2016). The spatial distribution of the diffuse CO_2 soil gas and temperature spots was partly influenced by uneven grounds. The equipment consists of a cylindrical metal vase (the chamber), a Licor® Li-820 Infra-Red spectrophotometer, an analogical-digital converter, and a palmtop computer. The accumulation chamber has a basal area of 200 cm^2 and an inner volume of 3060 cm^3 and is equipped with a ring-shaped perforated collector connected to a low-flow pump (20 $mL \cdot s^{-1}$). The pump permits to convey the soil gas from the chamber to the spectrophotometer and the re-injection of the circulating gas into the chamber guarantees the mixing of the soil gas by also minimizing the effect produced by the pumping action. The Infra-Red detector has a sensor operating in the range of 0-20,000 ppm of CO_2 with an accuracy of 4%. The signal is transformed by the analogical-digital converter and transmitted to the palmtop computer equipped with the Palm Flux 5.36 software, where a CO_2 concentration vs. time diagram is plotted in real-time. The instrument used in this work has a detection limit of ~0.08 g m^{-2} d^{-1} (https://www.westsystem.eu/it) and was calibrated before the fieldwork utilizing a laboratory calibration curve. The latter allowed to convert the temporal variation of the CO_2 concentration inside the chamber (dC_{CO2} dt^{-1}, expressed in ppmV/s), into the CO_2 flux (ϕCO_2, expressed in g m^{-2} d^{-1}), through a correlation factor (*cf*) obtained from the slope of the linear best-fit line of ϕCO_2 vs dC_{CO2} dt^{-1}. The measured ϕCO_2 was thus computed according to the following equation (e.g., Tassi et al., 2013; Cabassi et al., 2021):

$$\phi CO_2 = cf \times dC_{CO2}\, dt^{-1}$$

4.2 CO_2 and temperature data processing, spatial distribution, and CO_2 output estimation

The CO_2 flux and temperature data were processed using statistical and geostatistical methods to explore their spatial distribution and the origin of the CO_2 diffuse emission. The data were analyzed by using the Graphical Statistical Analysis (GSA) method (Chiodini et al., 1998), according to the procedure proposed by Sinclair (1974). The presence of multiple sources results in a polymodal distribution of the values, displaying a curve with one or more inflection points on a probability plot. The GSA method consists of the subdivision of these distributions into individual populations characterized by different proportions in the dataset, mean and median values, and standard deviations.

The distribution maps of both soil CO_2 flux and temperature were constructed using the log-normal Kriging interpolation method (e.g., Krige 1951; Matheron, 1970) using the Isatis© software package of Geovariances. The methodology involved the realization of an experimental variogram and the selection of the best fitting mathematical model for each variable. The fitted models were then cross-validated with the experimental data to check the performance of the model for kriging. The maps were then graphically reported using the QGIS software.

The total CO_2 output was calculated by applying Sichel's t-estimator (Mi) (David, 1977). The estimation was derived by multiplying Mi times the area covered by the population. In the same way, the central 95% confidence intervals of the CO_2 output were used to calculate the uncertainty of the populations.

4.3 Field work and Discrete Fracture Network surveys

A new field mapping of about 10 km^2 at a 1:5000 scale (Fig. 2) and collection of structural data in the most favorable exposures were carried out to obtain information on the geological and structural setting of the study area. Furthermore, the fracture distribution across the fault zone, where the geothermal manifestations are concentrated, was investigated to reconstruct the interplay between brittle deformation, fracture enhancement, and gas escaping. A detailed analysis of the fracture distribution was carried out in a key outcrop where highly fractured and hydrothermalized Jurassic siliceous beds of the Diaspri Fm (Tuscan Domain) are exposed in an abandoned quarry within "Le Biancane" natural park (Figs. 2 and 5).

In the field, fracture parameters (orientation, length, linear fracture intensity, mechanical aperture) were obtained through the scanline and scan area methodology. Most data were collected along a 25 m long scanline crossing the studied fault zone exposed in the main wall of the abandoned quarry (Fig. 5). Six additional scanlines, 1-2 m long each, were also performed: four scanlines were located at the same scarp of the main scanline; the other two scanlines were settled in different sites at about 30-40 m NW from the main scanline (Fig. 5). Scan areas (~1 m^2) were performed on the few pavement views allowing the measure of the fractures network in plain view (SL A and G in Fig. 5).

The first step of our fracture analysis consisted of clustering the fracture network. Since most of the fractures observed in the field are about normal to bedding, the fracture clustering was evaluated also considering the fracture setting after having reported bedding to its horizontal attitude, independently by the cause that determined the bedding rotation (Zambrano et al., 2016). By doing so, different fracture sets or families based on their orientation were defined. For each fracture set, the mean orientation (azimuth, dip) and the Fisher's K dispersion parameter (Fisher, 1953), were calculated. For the DFN modeling, all fracture families were modeled considering the current orientation measured in the field.

The fracture length (defined as the trace of the fracture on the bedding plane) distribution for each family was derived from the pavements scan areas analysis. Similarly, the fracture height (defined as the trace of the fracture on a vertical view) distribution was obtained from the scanlines performed on the walls. The aspect ratio (length/height) was estimated by considering the average of both properties. The volumetric fracture intensity (*P*32, defined as the total surface area of fractures planes per unit of volume) was derived by using the simulation-based workflow, proposed by Golder Associated Ltd. (2009) and already applied by other authors (e.g., Antonellini et al., 2014; Korneva et al., 2015; Zambrano et al., 2016). This consists in generating a minimum number of three DFN models with fixed fracture parameters (orientation, length distribution, aspect ratio) and variable input volumetric intensity (*P*32). The linear fracture intensity (*P*10) is defined as the number of fractures

divided by the length of the scanlines normal to the fracture set (Terzaghi, 1965). By this, the ratio *P32/P10* is obtained by linear regression (Dershowitz and Herda, 1992).

The hydraulic aperture, *e* (defined as the idealized fracture aperture for smooth parallel plates model; Snow, 1965), was derived from the mechanical aperture (*E*), by using the equation of Barton et al. (1985):

$$e = \frac{E^2}{JRC^{2.5}}$$

The JRC parameter was measured by visually comparing the fracture surface with a standard set of roughness profiles given by Barton and Choubey (1977). The mechanical aperture (*E*) of fractures was measured using a comparator with an accuracy of 0.01 mm.

Finally, stochastic DFN models were built using MOVE™ software of Petroleum Experts® by introducing the parameters derived from the field analysis: i) orientation; ii) fracture length; iii) aspect ratio; iv) aperture. The DFN models (35 x 48 x 3 m, with the largest size oriented N330º, and one-meter cell size) were generated to represent the documented fracture network (Fig. 5), computing both fracture porosity and geometric-based permeability tensor (Oda, 1985). Since most of the fractures crossing the chert beds are not vertically connected, a final correction was made to introduce in the model the rhythmically interbedded shaly levels, assuming for the latter an estimated permeability of 10^{-17} m^2 and a near 20% of the total thickness. Regarding the vertical component of the permeability, the weighted harmonic mean between both lithofacies (i.e., cherts and shaly levels) was computed, whereas the arithmetic mean was used for the horizontal components (Antonellini et al., 2014). The contribution of the permeability associated with fault parallel non-stratabound fractures located in the proximity (0.5 m) of the fault surface was not affected by such a correction, due to the tendency of these fractures not to affect the first mechanical boundary (bedding). The results of cells along the main vertical wall were extracted to compare the fracture parameters (i.e., fracture intensity, porosity, and permeability) with the output of the geochemical survey (i.e., soil temperature and CO_2 natural emissions).

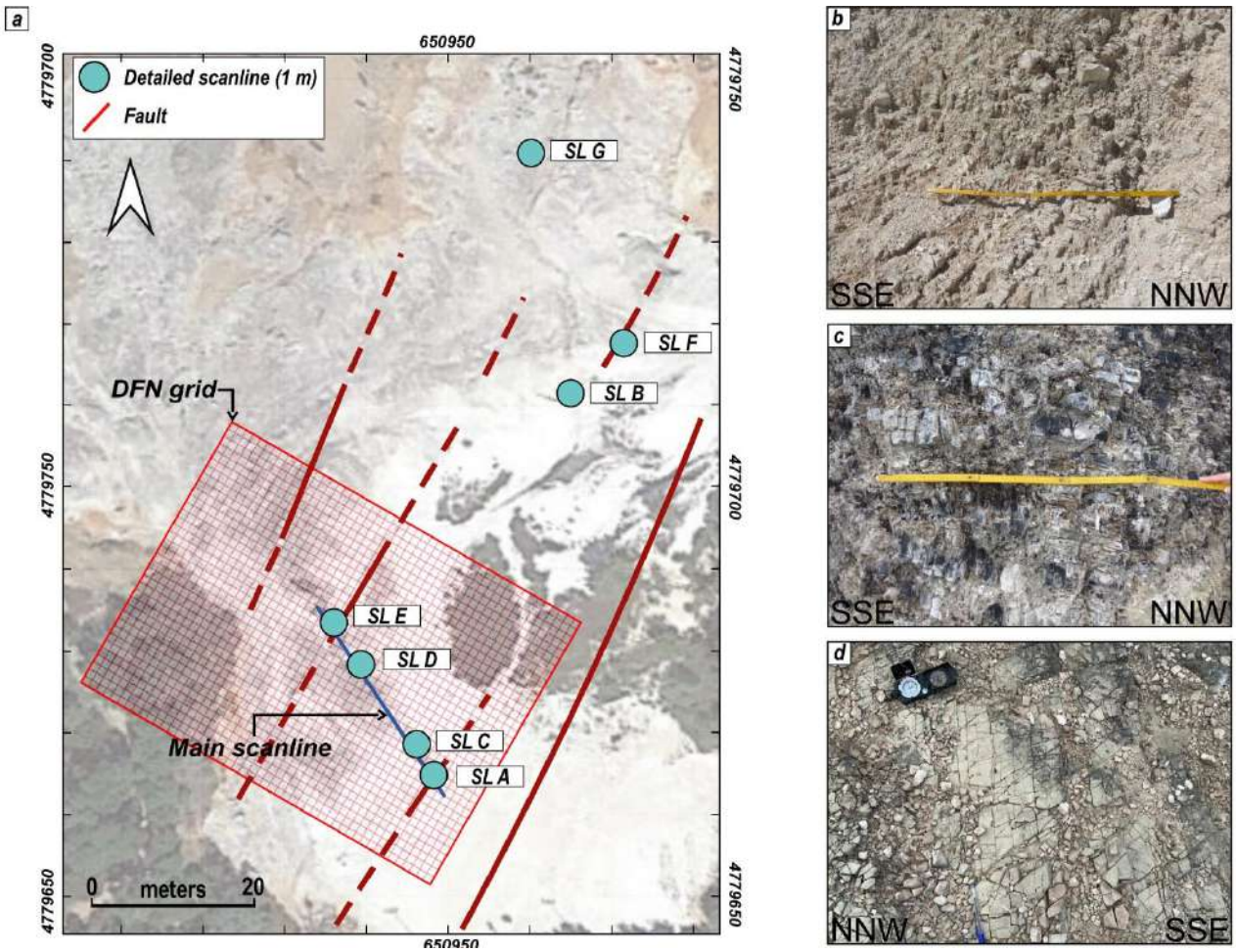

Figure 5. a) Map showing location of scanlines, DFN grid and the main faults affecting the area. The grid of the DFN model was oriented to follow the main orientation (N30°) of the observed faults. A main scanline (blue line) was performed along the scarp following the better exposure of the fracture and fault networks, as well as the main geothermal manifestations. Detailed scanlines (from A to G; turquoise circles) were located along the main scanline and in different areas. b-c) Examples of fractures measured along scanline A (b), scanline E (c); d) example of fracture setting plain view.

5. Results

5.1 Diffuse fluxes and soil temperature

Soil CO_2 fluxes ranged from 0.37 up to 2,927 g m^{-2} d^{-1}, with mean and median values of 197 g m^{-2} d^{-1} and 44.5 g m^{-2} d^{-1}, respectively, and standard deviation of ± 437 g m^{-2} d^{-1}. The cumulative frequency plot (Fig. 6a) of the CO_2 data shows two inflection points at LnϕCO_2 2.89 g m^{-2} d^{-1} (i.e., 18.1 g m^{-2} d^{-1}) and LnϕCO_2 5.65 g m^{-2} d^{-1} (i.e., 285.6 g m^{-2} d^{-1}). Population A represents 40% of the dataset with values ranging between 0.37 and 18.1 g m^{-2} d^{-1} with mean and median values of 5.0 g m^{-2} d^{-1} and 2.76 g m^{-2} d^{-1}, respectively, while the standard deviation is ± 5.04 g m^{-2} d^{-1}. Population B (43%) ranges from 21.4 and 285.6 g m^{-2} d^{-1}; the mean, the median, and the standard deviation are 95.7, 82.1 and ± 65.4 g m^{-2} d^{-1}, respectively. Finally, Population C includes 13% of the measurements and ranges from 390.3 and 2,926.7 g m^{-2} d^{-1}, with mean and median values of 874.8 g m^{-2} d^{-1} and 642.3 g m^{-2} d^{-1}. The standard deviation is ± 732.3 g m^{-2} d^{-1}.

Soil temperature data approximate a (Log)normal distribution, as highlighted by the cumulative frequency plot in Figure 6b. Values span over a wide range (from 24.8 up to 98.8 °C), with mean, median and standard deviation values of 46.4 °C, 42.2 °C, and ± 17.1 °C, respectively.

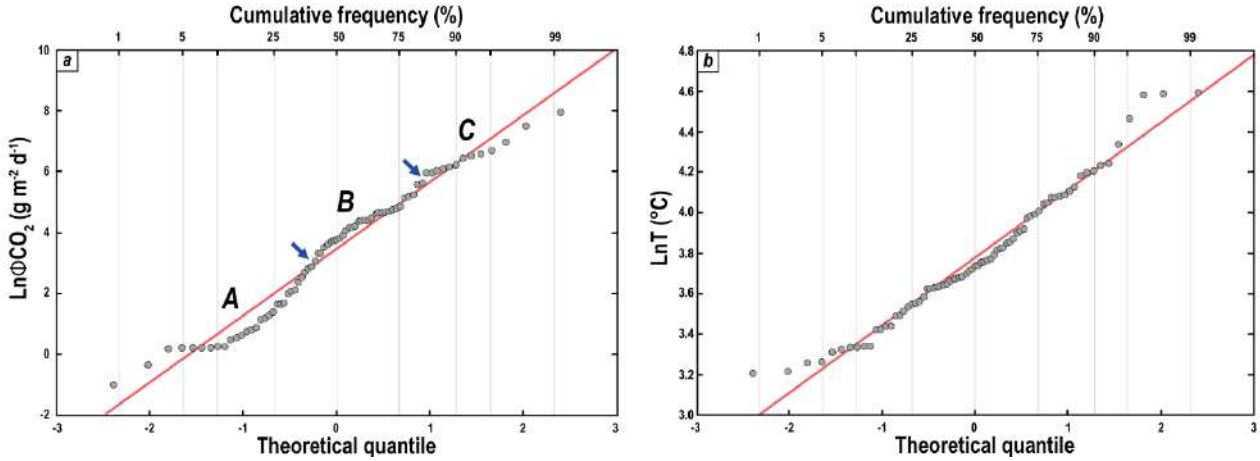

Figure 6. Cumulative frequency plots of the (a) soil CO_2 and (b) temperature measurements.

5.2 CO_2 output estimation

By applying Sichel's t-estimator for the CO_2 output in the studied area, a value of 0.21 t d^{-1} was computed (lower and upper confidence limits 0.17 and 0.29 t d^{-1}, respectively), essentially due to population B (0.06 t d^{-1}) and C (0.15 t d^{-1}), being the contribution of population A (i.e., <0.001 t d^{-1}) negligible. The normalized total CO_2 flux from the soil (i.e., the total output divided by the area of the survey) was 155.5 t d^{-1} km^{-2}. The percentage contribution of each population constituting the whole dataset is reported in Table 1.

Table 1. *Percentage contribution of each population constituting the whole dataset used to estimate the total amount of ϕCO2 released from the study area.*

Variable	Surface area (m^2)	Population	Measurements (n.)	Total output (t d^{-1})	95% Confidence interval (t d^{-1})
ϕCO_2	1350	A	30	<0.001	-
		B	32	0.06	0.05-0.08
		C	12	0.15	0.12-0.21
		Outlier	1	-	-
		Total	*75*	*0.21*	*0.17-0.29*

5.3 Distribution maps

The soil CO_2 flux and temperature distribution maps obtained by the kriging interpolation method are reported in Figure 7 (interpolation grid 1 x 1 m). The combination of three basic structures (2 Spherical plus Nugget effect) is the best model to describe the spatial variability of ϕCO_2 whereas the soil temperature spatial variability is best described by one spherical variogram. Variograms, variograms parameters, cross-validations of the mathematical model describing the experimental variogram of each map, standard deviation maps, and the measured values, are reported in the Supplementary Material.

CO_2 flux and temperature show a moderate spatial correlation, with the upper values of both parameters located in the northern, central, and southwestern sectors of the study area while the lowest ones mostly pertain to the easternmost zone (Fig. 7). In general, the highest CO_2 fluxes (up to 2927 g m^{-2} d^{-1}) and temperatures (up to 98.8 °C) are found in the central portion of the NW-oriented scarp that crosscuts the area, where the main structural lineaments have been found.

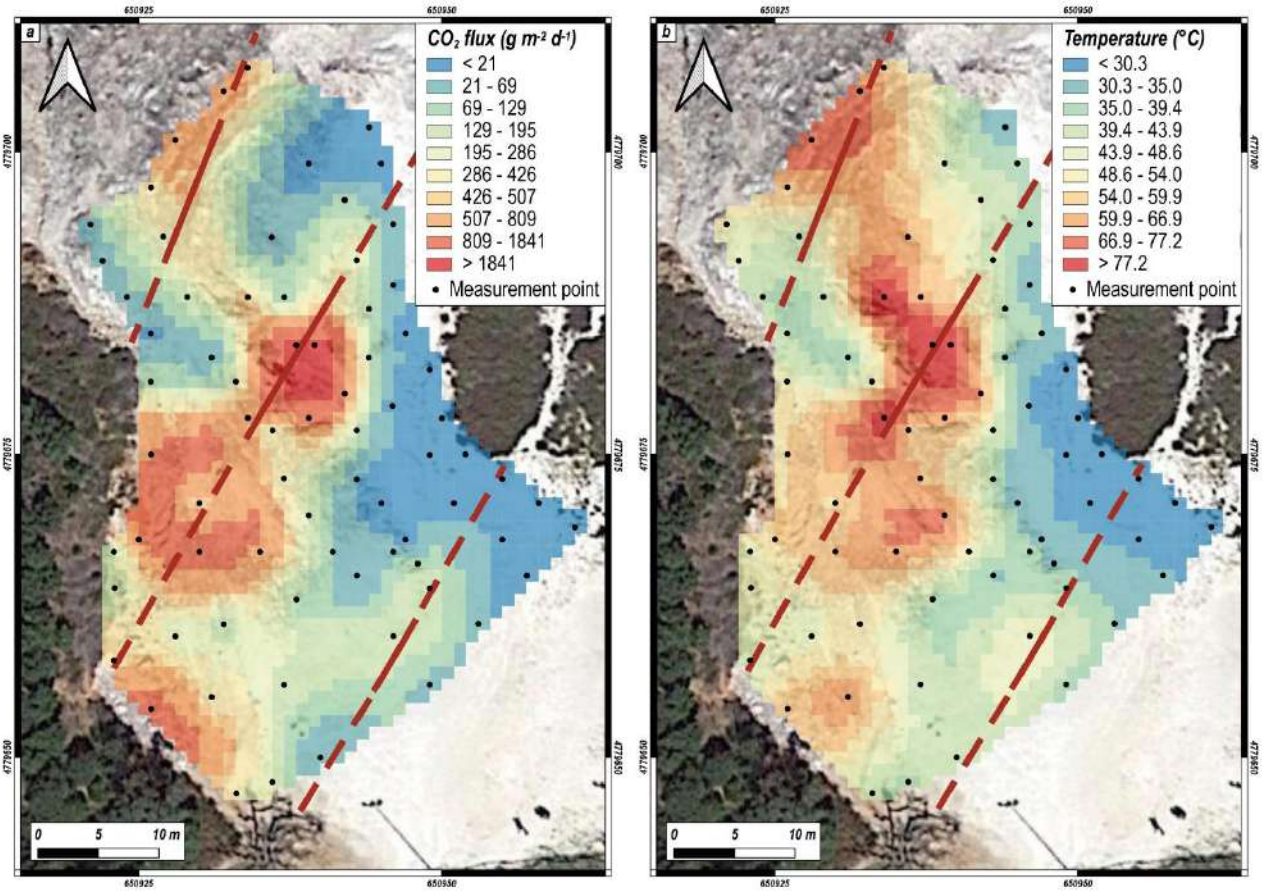

Figure 7. a) Soil CO_2 flux, and b) temperature distribution maps. Faults are reported as red lines.

5.4 Structural setting, fracture, and permeability analysis

An NNE-striking fault zone (the MMSP) crosses the study area (Figs. 1 and 2). This structure is at least 5 km long (Figs. 2 and 3) and is part of the NNE-trending fault system defining the transfer zone affecting the Larderello geothermal area (Liotta and Brogi, 2020). In the southern part, MMSP bounds the Neogene sediments filling the Lago Basin, whereas in the northern part it defines a splay of a NE-striking fault passing through the Larderello and Montecerboli villages (Fig. 2). In the area between Monterotondo Marittimo and Sasso Pisano villages, the fault zone consists of several subparallel and/or anastomosed NNE- and N-S-striking fault segments, dissecting the Jurassic-Tertiary succession of the Tuscan Nappe (Fig. 2). Steam and CO_2 emissions, hydrothermal alteration and silicization phenomena characterize the damage volumes of those fault segments affecting the Jurassic radiolarite (Diaspri Fm) (Fig. 8a) and the early Cretaceous limestone (Maiolica Fm). The geothermal manifestations mainly occur along an area between Monterotondo Marittimo and Sasso Pisano villages (Figs. 2, 3, and 4), thus indicating the trend of the main fault zone. This fault zone

was the object of geothermal exploration during the past decades (Lazzarotto, 1967; Lazzarotto and Mazzanti, 1978; Minissale, 1991; Batini et al., 2003; Bertini et al., 2006; Romagnoli et al., 2010) and today, is still producing the steam feeding the power plants (www.arpat.toscana.it).

At the map scale, the main fault zone involves the Tuscan Nappe and separates the hanging wall, made up of the late Oligocene-early Miocene quartz-feldspar micaceous sandstone (Macigno Fm) with its basal Cretaceous-Oligocene shaly succession (Scaglia Toscana Fm), from footwall consisting of the basal carbonate-siliceous succession (Fig. 2). This latter fault block comprises two main Tuscan Nappe sub-units doubled during the collisional phase of the Northern Apennines. The lower one is characterized by an exposed succession encompassed between the late Triassic evaporite (Burano Fm) and the Macigno Fm; this succession exhibits a significant tectonic omission resulting in the direct superimposition of the Macigno Fm on the early Jurassic massive limestone (Calcare Massiccio Fm) (Fig. 2b). The upper sub-unit is represented by a few klippen formed by a succession comprised between the Calcare Massiccio Fm and the Macigno Fm (Fig. 2b). Subligurian and Ligurian Units directly overlie both sub-units, thus implying a robust tectonic omission having affected the original stacked units.

The main fault zone is well exposed in a sector of the “Le Biancane” natural park in the wall of abandoned quarries (Figs. 4a and 8b). The tens meters-thick fault zone consists of sub-vertical secondary faults striking N20-30° (Fig. 8b-e), clearly associated with the visible emission of vapors. The protolith is composed of the Jurassic siliceous beds (Fig. 8a). This succession is mainly characterized by thin (average 4-15 cm), whitish to brownish stratified chert beds rhythmically interbedded with shaly levels up to 1 cm thick. Some chert beds are pure and vitreous, while others are composed of radiolarian (packstone to grainstone) chert often laminated at the base of the strata. This succession is overlain by about 10 m of slightly calcareous radiolarian chert beds, thinly bedded (average 4-6 cm), highly siliceous passing to whitish to reddish limestones interbedded with shaly levels about 0.5-1 cm thick. Cherty beds are intensely fractured (up to 5-6 fractures per 10 cm), although these fractures are confined within the cherty beds without cutting the shaly levels separating the different siliceous beds (Fig. 8).

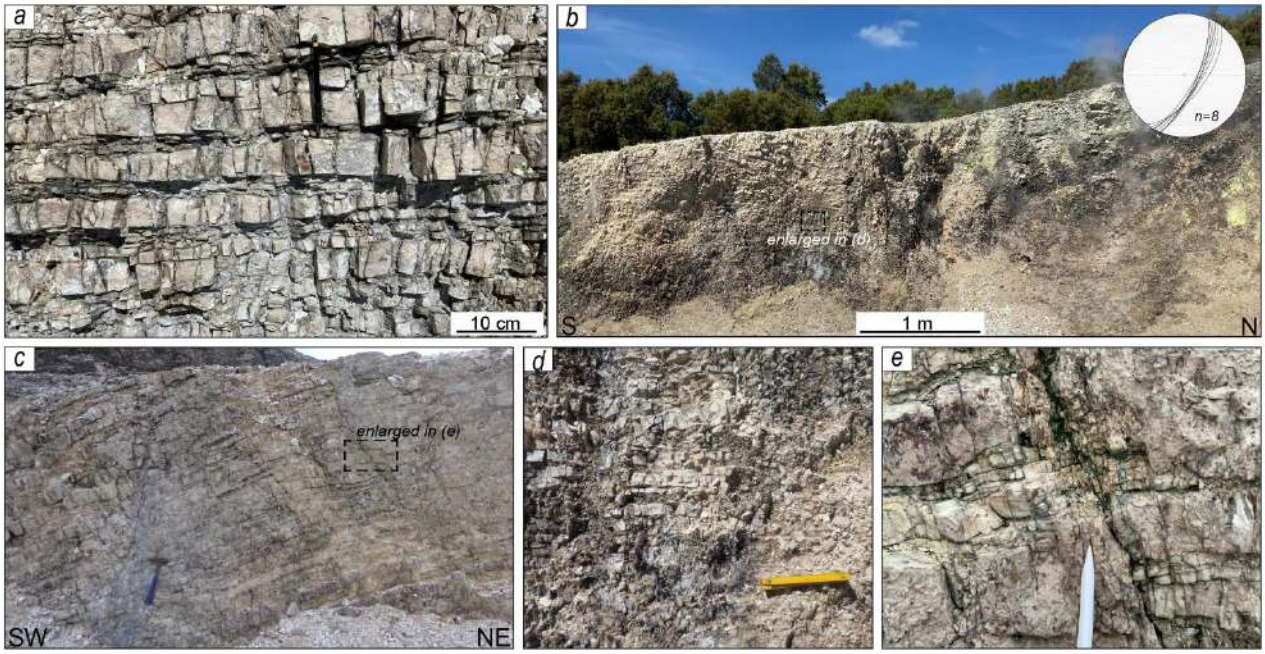

Figure 8. a) Photograph of the Jurassic siliceous beds (Diaspri Fm) exposed in the study area; b) panoramic view of the main fault zone exposed along the scarp (Fig. 5a); c) panoramic view of a minor fault exposed in the study area; d) detail of the fault zone showing highly fractured and altered (dark zones) Diaspri Fm due to the intense geothermal activity occurring along the fault zone; e) detail of the shale and siliceous beds cut by a minor fault.

The fractures were classified in families for modeling purposes. The grouping was based on the orientation and type of the fractures (joints, faults) (Fig. 9). We have considered fractures likely predating, or coevally formed during tilting of beds, as the ones clustering in stereonets after applying the bed restoration (normal to bedding), whereas fractures formed after the tilting, clustered better on the current orientation. From the fracture analysis seven families were differentiated (Table 2). For the DFN modeling, the current fracture orientation was used for each scanline (Fig. 9c).

Table 2. *Main fracture families differentiated from the scanlines.*

Set	Type	Orientation				Notes
		Dip direction (°)	*Strike (°)*	*Mean dip (°)*	*Fisher (K)*	
1	Joint	167	77	84	39	After rotation
2	Joint	107	17	80	65	After rotation
3	Joint	245	155	85	125	After rotation
4	Joint	204	114	87	126	After rotation
5	Fault related Joint	127	37	69	103	Without rotation
6*	Shear joints/Fault	120	30	85	200	Without rotation
7*	Shear joints/Fault	220	130	85	200	Without rotation

Notes: Set 6* represents fault-parallel, non-stratabound fractures strictly located in the proximity of the fault surface

The apertures of the fractures range from 0.05 mm to 0.1 mm, which agree with the narrow beds (generally <20 cm). The other geometric features are summarized in Table 3. Fracture intensity is relatively high and tends to increase towards the main fault surface located to the north of the model,

consistent with the field observations. Some scattering and picks in this trend are related to the presence of secondary fault structures, whereas zones with undetected fractures are related to cementation and alteration.

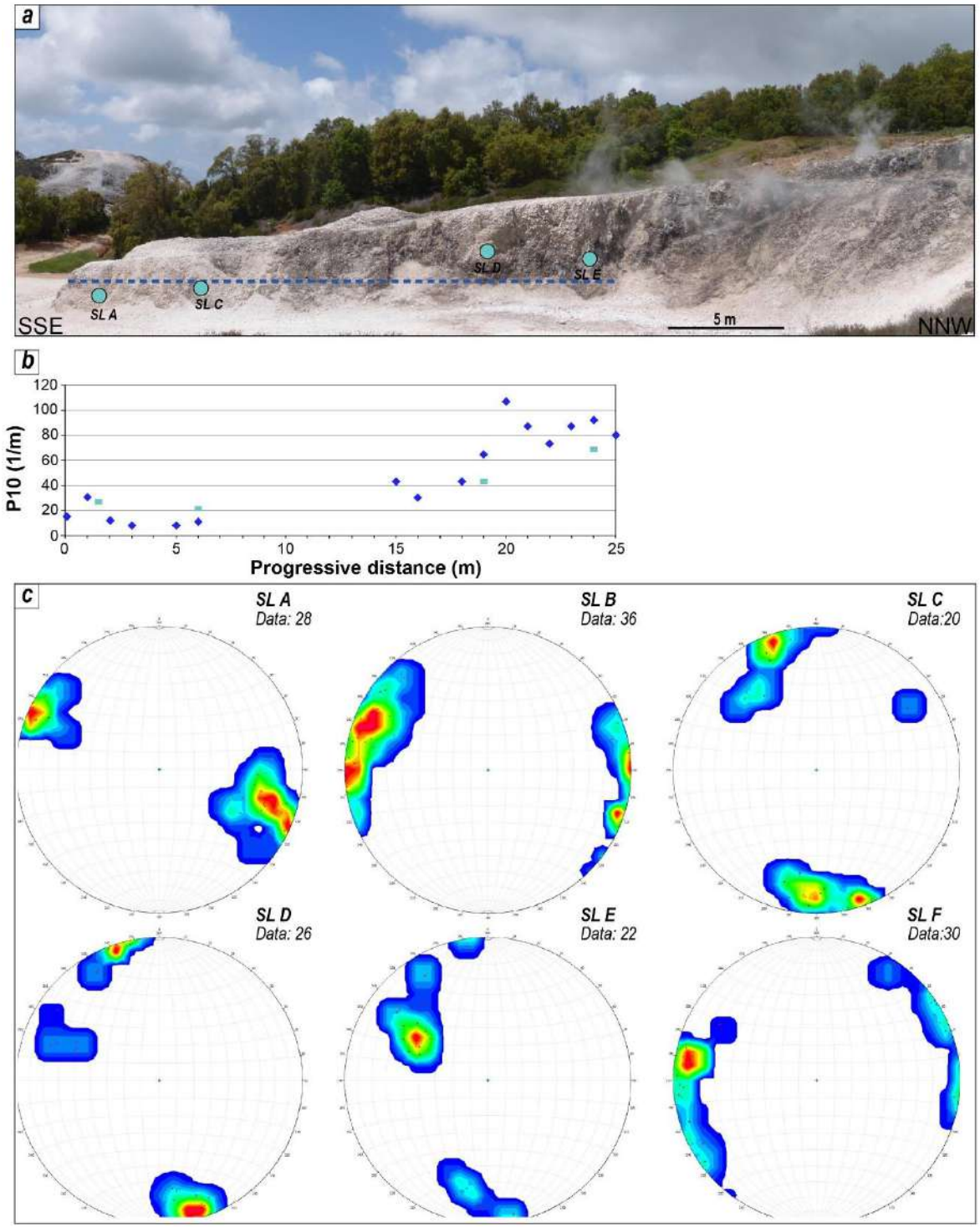

Figure 9. a) Panoramic view of the scarp where the main scanline (dashed blue line) and the detailed scanlines (SL A, SL C, SL D, SL E) were performed; b) linear fracture intensity *P*10 along the main scanline indicated in (a); c) stereoplots of the fractures (poles of planes) measured in each of the indicated Scanline.

The secondary fault structures have from a few centimeters of displacements to a few meters of offsets. The upscaled hydraulic properties (porosity and permeability) follow the same trend provided by the linear fracture intensity. The porosity is lower than 0.1% of the whole volume, whereas the permeability is generally lower than 10^{-13} m^2. The permeability values of the sector with evident steam area emission and those with apparent no emissions (near the gas manifestations) are one order of magnitude higher than the area without visible manifestations of steam. The permeability tensor parallel to the trend of the study fault zone is near double of the other components.

Table 3. *Fractures geometric attributes used for DFN models construction.*

Set	Length (cm)				Aspect ratio	Fracture intensity		
	Min	*Max*	*Mean*	*St. Dev.*		*P*10 Mean	*P*10 St. Dev.	*P*32/*P*10
1	5	20	10.0	3	1.4	24.4	3.3	1.1
2	5	20	10.0	3	1.4	25.1	18.4	1.1
3	5	15	7.0	2	1.0	9.8	3.3	0.8
4	5	15	7.0	2	1.0	7.4	3.6	0.8
5	3	10	5.0	2	0.7	8.6	7.8	0.6
6*	-	-	6.0	-	2.0	5.0	-	1.0
7*	-	-	2.5	-	2.0	1.0	-	1.0

Notes: the aspect ratio is provided for an average bed thickness of 7 cm. The geometrical properties of the set 6 and 7 are estimated since are out of scale at the outcrop.

6. Discussion

6.1 Origin and transport of soil CO_2 degassing

The cumulative frequency plot (Fig. 6) has allowed identifying the presence of different populations of CO_2 fluxes, suggesting three distinct sources or transport mechanisms of carbon dioxide characterized by threshold and mean values of the same order of magnitude as those recognized by Cabassi et al. (2021) in the southern part of the “Le Biancane” natural park (Fig. 3). The low-flux population (A) shows mean and upper threshold values of ~5 and ~18 g m^{-2} d^{-1}, respectively, and indicates a biological source (i.e., plant and microbial respiration and organic decomposition; Raich and Schlesinger, 1992; Cardellini et al., 2003; Chiodini et al., 2008; Viveiros et al., 2010, 2020). Population C is likely related to a hydrothermal source, being the CO_2 values >390 g m^{-2} d^{-1} (e.g., Viveiros et al., 2010, 2020). Consequently, population B can be linked to mixing processes, to different degrees, between populations A and C. However, when the CO_2 flux and the corresponding $\delta^{13}C$-CO_2 data of Venturi et al. (2019), collected 100 m far from the study area of the present work, are plotted against each other (Fig. 10) the lowest fluxes (<~20 g m^{-2} d^{-1}) show wide variability in terms of carbon isotopes, from -16.1‰ up to -0.53‰, the latter being much heavier than a purely biogenic CO_2 (e.g., Sharp, 2017). This relatively large isotopic interval can be due to different fractionation processes such as mixing between biogenic (e.g., −33 to −23‰ for C3 plants; Sharp, 2017) and hydrothermal (e.g., the Larderello geothermal reservoir; Gherardi et al., 2005) sources, diffusive transport (Federico et al., 2010), and microbial consumption at shallow depths (Venturi et al., 2019) or methanogenic processes which occur in the hydrothermal reducing environment

(Whiticar, 1999). Regardless of the origin of CO_2, fluxes >~20 g m^{-2} d^{-1} show a clear hydrothermal isotopic signature. However, when ϕCO_2 values comprised between ~20 and ~300 g m^{-2} d^{-1} are considered, the carbon isotopes reach significantly high values (up to +3.41‰). These strikingly positive values are likely associated with a two-stage fractionation process due to boiling during fluid ascent within the reservoir and a subsequent isotopic enrichment as CO_2 diffuses through the soil (Rissmann et al., 2012). In this way, fluxes ranging between ~20 and ~300 g m^{-2} d^{-1} likely suggest that diffusive and advective transport processes may occur simultaneously. Fluxes higher than ~300 g m^{-2} d^{-1}, associated with soil temperature >53 °C, seem to be linked to a purely advective transport, although a microbial CO_2 uptake and fixation positive shift occur (Venturi et al., 2019; Fig. 10).

Based on the: i) proximity of our and Venturi et al. (2019) study areas, ii) tectonic setting and iii) hydrothermal evidence (Figs. 2 and 3), the CO_2 emissions from both areas can be assumed to be governed by the same geochemical processes. The ϕCO_2 intervals identified in Fig. 10 from Venturi et al. (2019) data (i.e., <20; 20-300; >300 g m^{-2} d^{-1}) well agree with those identified in the study area distinguishing the three populations of fluxes (Fig. 6). In this context, fluxes of population A (i.e., <18 g m^{-2} d^{-1}; Fig. 6) are likely linked to a purely diffusive transport driven by a concentration gradient, while population C data (>390 g m^{-2} d^{-1}; Fig. 6) are driven by an advective transport related to a pressure gradient. Soil CO_2 fluxes between 21 and 290 g m^{-2} d^{-1} (Population B; Fig. 6) can be regarded as representative of a combined diffusive–advective transport mechanism.

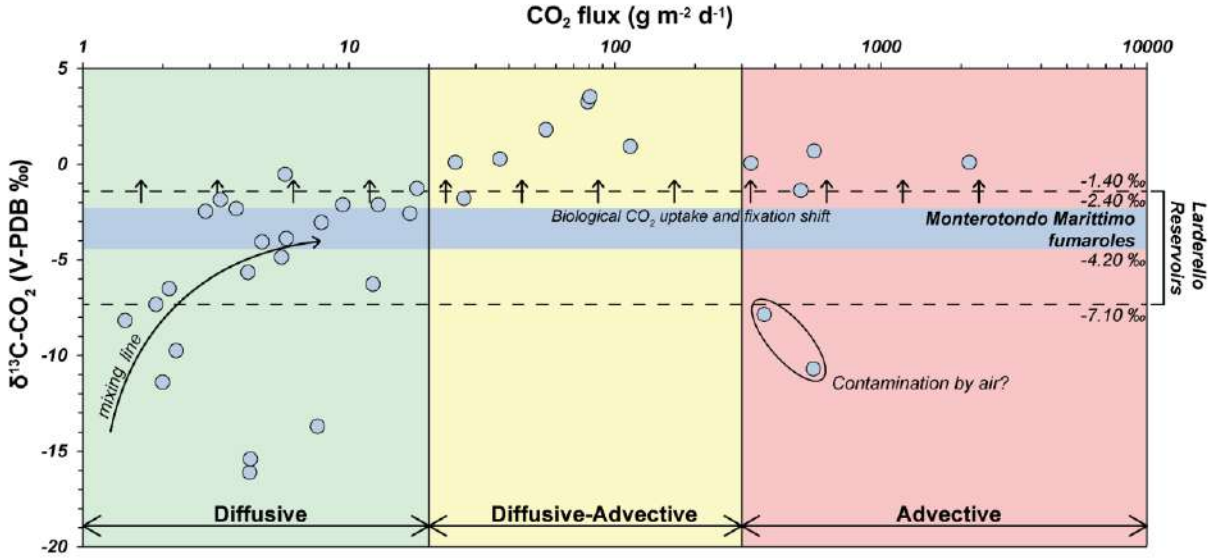

Figure 10. Soil CO_2 flux vs. isotopic composition of fluxes from the Monterotondo Marittimo area (data from Venturi et al., 2019). $\delta^{13}C$-CO_2 composition of Monterotondo Marittimo fumaroles (Venturi et al., 2019; Leila et al., 2021) and Larderello reservoirs are also reported (Gherardi et al., 2005).

6.2 Correlation between faults/fractures and fluid emissions

In the “Le Biancane” natural park area, the exposed rocks are highly fractured as revealed by the significantly high values of *P*32. The fractures are limited to the cherty beds, about 7 cm thick, whereas they do not (or rarely) affect the interbedded shaly layers that are playing the role of mechanical boundaries (Fig. 11a). Only a few fractures, most likely incipient fault planes, cut both

the shaly and cherty beds. These features have been mostly found near main fault slip surfaces and are responsible for localized vertical connectivity of the fracture network (Fig. 11b,c). With respect to the fracture sets, seven families of fractures were differentiated; one of them seems to be strictly fault-related by considering its orientation and field observations, while two of them are incipient faults. In terms of fracture density, most of the families of fractures are more abundant towards the fault slip surfaces, while other families are more unevenly distributed. The reason behind this setting is probably related to two concomitant factors: i) inherited fracture network pre-dating the fault activity, and ii) a deformation history of the fault zone related to the diachronic activation of the fault segments in a setting of progressive deformation.

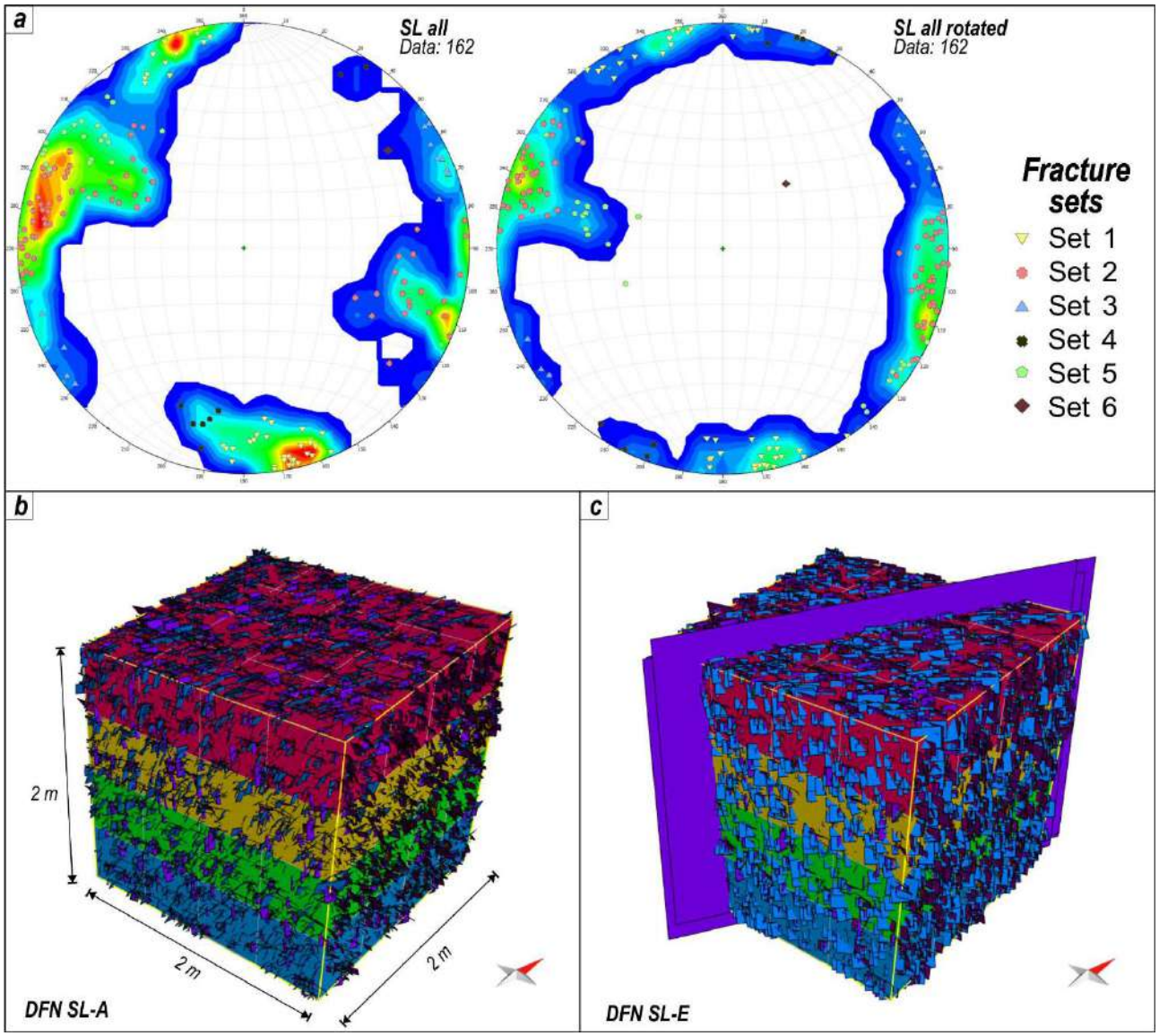

Figure 11. a) Stereonet data from all the scanlines with and without rotation; b) detail of the DFN models in proximity of the (b) scanlines SL A and (c) SL E. Most of the modelled fractures are stratabound, however near secondary faults non-stratabound fractures parallel to faults N30° striking are present (purple).

In terms of vertical pathways for CO_2, the main conduits are represented by the localized pervasive fault-related fractures. Actually, the highest CO_2 fluxes (i.e., >300 g m^{-2} d^{-1}), likely related to a

pressure-gradient controlled transport (Fig. 10), were mainly measured in correspondence with the NE-SW faults (Fig. 12a) characterizing the MMSP area (Figs. 2 and 3) which is part of the Larderello transfer fault system (Liotta and Brogi, 2020) (Fig. 1). This transfer fault system shows a compartmentalized permeability which is maximum in the tract comprised between Monterotondo Marittimo and Sasso Pisano, as indicated by the geothermal manifestations occurring only in this section (Figs. 3 and 4). Nevertheless, although these manifestations characterize the whole fault zone between Monterotondo Marittimo and Sasso Pisano localities, the maximum CO_2 fluxes are mainly concentrated in the "Le Biancane" area (Venturi et al., 2019; Leila et al., 2021; Cabassi et al., 2021) (Figs. 3 and 7). Based on our dataset, this can be explained by the enhanced fracture permeability induced by the numerous fault segments (Figs. 2 and 3) which consist of anastomosed structures defining the first-order transfer fault zone (Fig. 2). While fault-related fractures enhance the vertical permeability along the fault strike, the diffuse stratabound fractures permit the CO_2 to migrate laterally. This explains why the geothermal manifestations are widespread in a large area around the fault zone, even distant from the fault-related fractures. Looking at the CO_2 flux and temperature distribution we observed a moderate positive correlation between the two parameters in both the whole analyzed area (Figs. 7 and 12b) and along the NW-striking transect that cross-cut the fault zone (Fig. 12c).

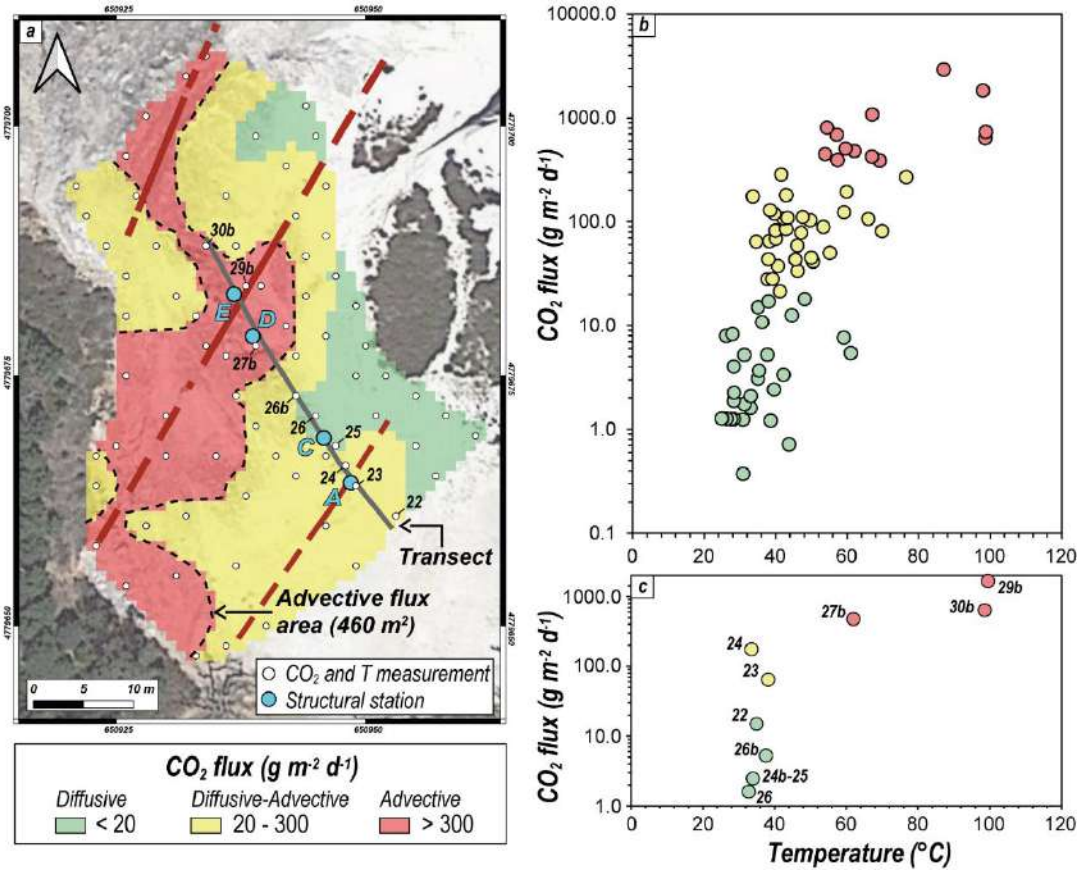

Figure 12. a) Distribution map of the soil CO_2 flux divided by the inferred transport mechanisms; b) relationship between soil CO_2 and temperature in the study area and c) along the transect in (a). Numbers in (a) and (c) represent the id of the measurement points reported in the supplementary material.

The correlation between geothermal soil degassing and fractures is noted by comparing the results of the DFN modeling along the same transect (Fig. 13), where CO_2 fluxes and soil temperatures are reported with *P*32 and permeability values. CO_2 fluxes and soil temperature behave similarly where the highest values of both parameters are found. In fact, in the north-western portion of the transect, in the proximity of the scanlines D and E (Fig. 5 and 12a), fluxes higher than 480 g m^{-2} d^{-1} are associated with soil temperatures >62 °C (and maximum up to 98.6 °C) (Figs. 12c and 13). These high emissions are linked to the enhanced fracture permeability within the fault damage zone, where *P*32 higher than 49 and up to 109, and permeability values up 9.29*10^{-14} m^2 (Fig. 13) were computed. The presence of sub-vertical, persistent slip surfaces and related damage zones striking N20-30° (Figs. 8, 11) would enhance the efficient advective ascent of high amounts of CO_2 and heat to the surface, driven by a pressure gradient (Fig. 10). The rapid rise of the gases would prevent the fractionation of the CO_2 isotopologues, thus maintaining the isotopic signature of the CO_2 source of the reservoir (Fig. 10) and favoring the rise of steam without appreciable condensation (Capasso et al., 2001; Camarda et al., 2007; Rissmann et al., 2012). This results in a high CO_2 emission and a sensible temperature anomaly at the surface, indicative of active hydrothermal circulation of geothermal fluids along deep-rooted fractures (Giammanco et al., 2016; Rolleau et al., 2017; Lamberti et al., 2019; Taussi et al., 2021).

Moving toward the central part of the transect (Fig. 13) where scanline C was analyzed (Fig. 5 and 12a), different structural features characterize the protolith. *P*32 and permeability values drop down to 2.65-2.76 and 2.74-2.64 *10^{-14} m^2, respectively (Fig. 13). At the same time, the measured CO_2 fluxes dramatically decrease down to <6 g m^{-2} d^{-1}, while soil temperatures are relatively constant (between 32.9 and 37.6 °C). The protolith is here affected by intense fracturing, although with a low persistence and a spatial development only limited to the siliceous beds without cutting the interlayered shale (Fig. 8). In this case, the poorly-connected fracture network favors the slow and concentration-driven movement of the CO_2, therefore, boosting the fractionation processes (Fig. 10; Camarda et al., 2007) at a medium-low temperature (i.e., slightly higher than the atmospheric one during the fieldwork).

A marked decoupling of CO_2 and temperature was observed in the south-western part of the transect (Figs. 12a and 13), far from the main slip surfaces. Here, the CO_2 fluxes are between 65 and 175 g m^{-2} d^{-1} while temperatures remain constant at about 34-38 °C. Near scanline A (Fig. 5 and 12a) – except for measurement #24 where an incipient fault is located – fracture network is characterized by relatively moderated volumetric fracture intensity (*P*32) and permeability values ranging between 68 and 70, and 5.76*10^{-14} and 6.03*10^{-14} m^2 (Fig. 13), respectively. This fracture setting permits a diffuse degassing, but the inadequate pressure of the geothermal fluids triggers the vapor condensation. A loss of heat, thus, occurs on the rising way through the not well-developed fractures (Giammanco et al., 2016) together with the dispersion of the ascending gas over larger areas – with consequent fractionation processes (Fig. 10) – taking advantage of the higher ground permeability (Fig. 13).

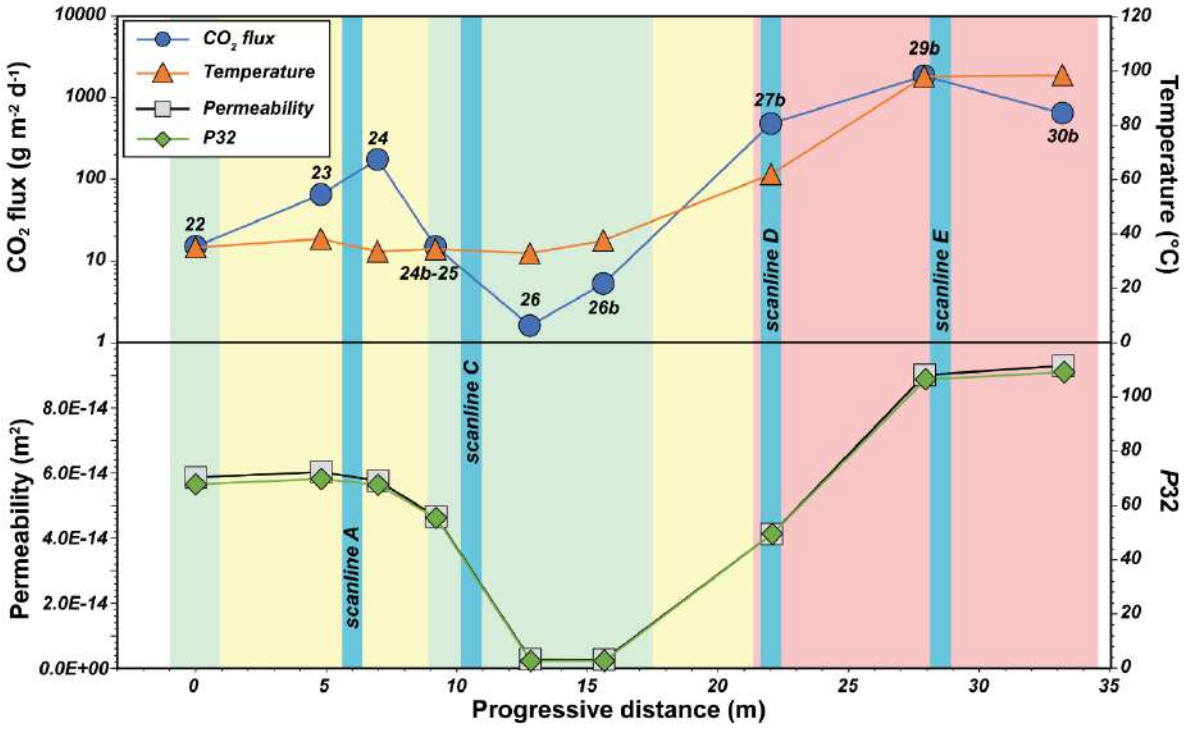

Figure 13. Soil CO_2 flux, temperature, *P*32 and permeability measurements carried out along the transect represented in Figure 12, which runs orthogonally to the fault zone of MMSP. The location of the detailed scanlines is also shown in turquoise. Background colors represent the main transport mechanism of CO_2; green: diffusive, yellow: mixed diffusive and advective, red: advective.

The structural setting has also implications for the quantity of CO_2 emitted from the investigated fault zone. The normalized CO_2 output from the whole studied area (1,350 m^2) was estimated at ~155 t d^{-1} km^{-2}, virtually equal to that computed by Cabassi et al. (2021). This value is much higher than the endogenous emission at e.g. Los Humeros (Mexico; ~52 t d^{-1} km^{-2}; Jentsch et al., 2020), Rotorua (New Zealand; 40-70 t d^{-1} km^{-2}; Werner and Cardellini, 2006) or Reykjanes (Iceland; ~53 t d^{-1} km^{-2}; Fridriksson et al., 2006), and on the same order of magnitude of e.g. Ischia and Latera (Italy; ~173 and ~112 t d^{-1} km^{-2}; Chiodini et al., 2004; Chiodini et al., 2007), Furnas (Azores; up to ~112 t d^{-1} km^{-2}; Viveiros et al., 2020) and Copahue (Chile-Argentina; ~175 t d^{-1} km^{-2}; Chiodini et al., 2015). However, when only the purely hydrothermal discharge (population C; Table 1) – estimated in 0.15 t d^{-1} – and the area characterized by the advective flux (460 m^2; Fig. 12) are considered, the value rises to 326 t d^{-1} km^{-2}, that makes it comparable to other large geothermal fields such as Ohaaki West and Rotokawa (New Zealand; ~307 and ~316 t d^{-1} km^{-2}, respectively; Rissmann et al., 2012; Harvey et al., 2015), confirming the pivotal role of the structural characters in the control of the fluid emissions.

7. Conclusions

The Monterotondo Marittimo-Sasso Pisano area stands at the border of the pull-apart Lago Basin, a regional active transfer zone characterizing the Larderello geothermal field (Liotta and Brogi, 2020). This structure acts as a preferential way for mantle-derived fluids ascent and permits the geothermal

fluids to be conveyed from the reservoir(s) to the shallower levels (Fig. 14a). The integration between CO_2 flux measurements and fracture distribution, crossing a sector of the transfer zone, indicates that fracture-induced permeability is the main factor in controlling the CO_2 local emission. A quantification of this implies permeability values in the order of 10^{-14} m^2 to permit degassing. Small variations of this value (from 1 to 8 $*10^{-14}$ m^2) influence the transport mechanism of CO_2, which can pass from diffusive to advective through the mixing of both processes (Fig. 14b). The diffusive transport mechanism is driven by a concentration gradient and characterizes those areas usually located far from the main shear zone (Fig. 14b,c), where fractures have a low persistence and are mainly limited to the stratabounds, thus indicating that the lateral migration of CO_2 is driven by layering (Fig. 14b,c). Differently, CO_2 advective transport is favored in the fault shear zone, where pervasive fractures that directly affect the reservoir (Fig. 14a) allow the rapid rise of high amounts of CO_2 and steam (Fig. 14b,c), avoiding $\delta^{13}C$-CO_2 fractionation of soil gas and maintain high temperatures. A combination of the diffusive and advective types of transport occurs in those transitional areas – or near the incipient faults (Fig. 14b) – where the influence of the main shear zone is still present. Here, fractures characterized by moderate persistence and intermediate permeabilities ensure a high degassing (Fig. 14b,c), but they do not prevent the vapor from condensation and heat loss. Finally, considering the regional setting, our results enforce the view that the transfer zones are favorable regional structures to localize the circulation of fluids, enhancing significant vertical permeability.

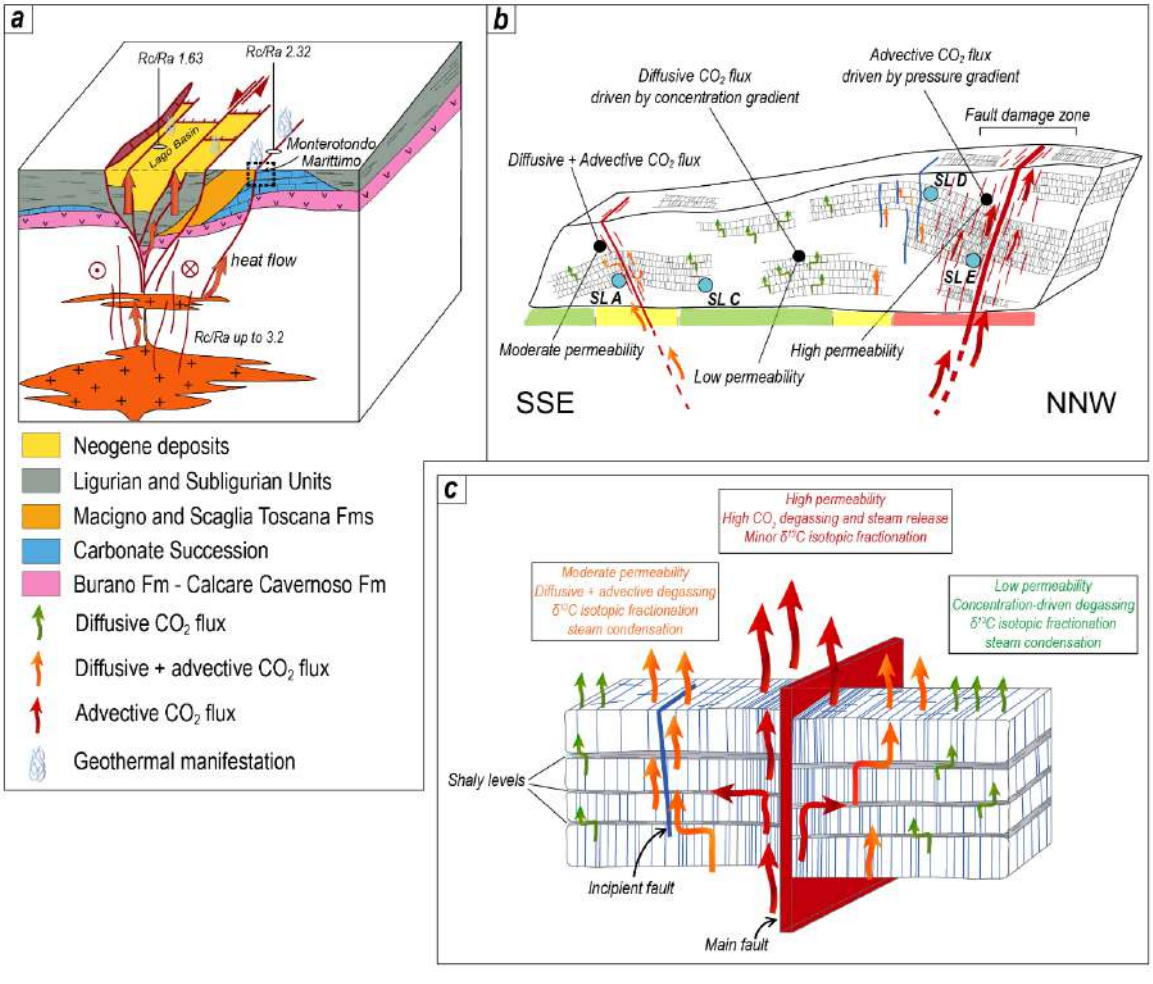

Figure 14. a) Geological sketch (not to scale) illustrating the tectonic and geothermal context of the Monterotondo-Sasso Pisano area, in the frame of the Lago pull-apart Basin developed within the transfer zone affecting the geothermal area of Larderello; b-c) local (b) and conceptual (c) models of the behavior of the CO_2 and steam emissions and transport mechanism, influenced by the enhanced permeability through the fault zone.

Acknowledgements

This work was partially financially supported by the laboratory of Stable Isotope Geochemistry of the Department of Earth Sciences and CNR-IGG of Florence. A.B., D.L., and M.Zu. received funding from the European Community's Seventh Framework Programme under grant agreement No. 608553 (Project IMAGE). M.Zu. received funding also from the Italian Ministry of University and Research (MIUR), through the program PON-AIM (Attraction and International Mobility) – project no. 1815472, Activity 1, line 1. The 3D fracture modeling was performed using Move™ educational licenses provided by Petroleum Expert Limited (PETEX) to the Department of Earth and Geoenvironmental Sciences of the University of Bari (contact L. Spalluto) and the Geology Division of the University of Camerino (contact M. Zambrano). M.T. is grateful to University of Urbino for funds received through a post-doc grant. G. Boschi is kindly acknowledged for his help during the sampling campaigns.

References

Agosta, F., Alessandroni, M., Antonellini, M., Tondi, E., 2010. From fractures to flow: a field-based analysis of an outcropping carbonate reservoir. Tectonophysics, 490, 197-213.

Agostinetti, N.P., Licciardi, A., Piccinini, D., Mazzarini, F., Musumeci, G., Saccorotti, G., Chiarabba, C., 2017. Discovering geothermal supercritical fuids: a new frontier for seismic exploration. Scientific Reports 7, 14592.

Anderson, T.R., Fairley, J.P., 2008. Relating permeability to the structural setting of a fault-controlled hydrothermal system in southeast Oregon, USA. Journal of Geophysical Research, 113, B05402.

Antonellini, M., Cilona, A., Tondi, E., Zambrano, M., Agosta F., 2014. Fluid flow numerical experiments of faulted porous carbonates, Northwest Sicily (Italy). Marine and Petroleum Geology, 55, 186-201.

Baldi, P., Bertini, G., Cameli, G.M., Decandia, F.A., Dini, I., Lazzarotto, A., Liotta, D., 1994. Tettonica distensiva post-collisionale nell'area geotermica di Larderello (Toscana meridionale). Studi Geologici Camerti 1, 183–193.

Barbier, E., 2002. Geothermal energy technology and current status: an overview. Renewable and Sustainable Energy Reviews 6, 3-65.

Barcelona, H., Maffucci, R., Yagupsky, D., Senger, M., Bigi., S., 2020. Discrete fracture network model of the vapor zone leakages at the Copahue geothermal field. Journal of Structural Geology 140, 104155.

Barchi, M.R., 2010. The neogene-quaternary evolution of the Northern Apennines: crustal structure, style of deformation and seismicity. In: In: Beltrando, M., Peccerillo, A., Mattei, M., Conticelli, S., Doglioni, C. (Eds.), The Neogene-Quaternary Evolution of the Northern Apennines: Crustal Structure, Style of Deformation, Seismicity 36 Journ. Virt. Explorer.

Bartole, R., 1995. The North Tyrrhenian-Northern Apennines post-collisional system: constraints for a geodynamic model. Terra. Nova 7, 7–30.

Barton, N.R., Choubey, V., 1977. The shear strength of rock joints in theory and practice. Rock Mechanics, 10 (1-2), 1-54.

Barton, N., Bandis, S., Bakhtar, K., 1985. Strength, deformation and conductivity coupling of rock joints. International Journal of Rock Mechanics and Mining Sciences & Geomechanics Abstracts, Vol. 22 (3), 121-140.

Batini, F., Burgassi, P.D., Cameli, G.M., Nicolich, R., Squarci, P., 1978. Contribution to the study of the deep lithospheric profiles: deep reflecting horizons in Larderello-Travale geothermal field. Mem. Soc. Geol. It. 19, 477–484.

Batini, F., Brogi, A., Lazzarotto, A., Liotta, D., Pandeli, E., 2006. Geological features of Larderello-Travale and Mt. Amiata geothermal areas (southern Tuscany, Italy). Episodes 26, 239-244.

Bellani, S., Brogi, A., Lazzarotto, A., Liotta, D., Ranalli, G., 2004. Heat flow deep temperatures and extensional structures in the Larderello Geothermal Field (Italy): constraints on geothermal. J. Volc. Geoth. Res. 132, 15–29.

Bentivegna, M., 2010. Il Patrimonio Geologico: una risorsa da proteggere e valorizzare. Geologia dell'Ambiente. Periodico della SIGEA (Società Italiana di Geologia Ambientale). Supplemento al n.2/2011 ISSN 1591-5352. Atti del Convegno Nazionale, 29-30 April, 2010, Sasso di Castalda – Potenza (Italy). (In Italian)

Bertani, R., Thain, I., 2002. Geothermal power generating plant CO_2 emission survey. IGA News, 49, pp. 1-3.

Bertini, G., Cameli, G.M., Costantini, A., Decandia, F.A., Di Filippo, M., Dini, I., Elter, F.M., Lazzarotto, A., Liotta, D., Pandeli, E., Sandrelli, F., Toro, B., 1991. Struttura geologica fra i monti di Campiglia e Rapolano Terme (Toscana meridionale): stato attuale delle conoscenze e problematiche. Studi Geol. Camerti Spec. 1, 155–178.

Bertini, G., Casini, M., Gianelli, G., Pandeli, E., 2006. Geological structure of a long-living geothermal system, Larderello. Italy. Terra Nova 18, 163–169.

Bianco, C., Godard, G., Halton, A., Brogi, A., Liotta, D., Caggianelli, A., 2019. The lawsonite-glaucophane blueschists of Elba Island (Italy). Lithos 348–349, 105198.

Billi, A., Salvini, F., Storti, F., 2003. The damage zone-fault core transition in carbonate rocks: implication for fault growth, structure and permeability. Journal of Structural Geology, 25, 1779-1794.

Brogi, A., 2020. Late evolution of the inner Northern Apennines from the structure of the Monti del Chianti-Monte Cetona ridge (Tuscany, Italy). Journal of Structural Geology 141, 104205. https://doi.org/10.1016/j.jsg.2020.104205

Brogi, A., Cerboneschi, A., 2007. Upper crust «boudinage» during post-collisional Miocene extension in Tuscany: insights from the southern part of the Larderello geothermal area (Northern Apennines, Italy). Geodin. Acta 20 (5), 327–351.

Brogi A., Liotta, D., 2008. Highly extended terrains, lateral segmentation of the substratum, and basin development: the middle-late Miocene Radicondoli Basin (inner northern Apennines, Italy). Tectonics 27, 1–20.

Brogi, A., Lazzarotto, A., Liotta, D., Ranalli, G., 2005. Crustal structures in the geothermal areas of southern Tuscany (Italy): insights from the CROP 18 deep seismic reflection lines. J. Volcanol. Geotherm. Res. 148, 60–80.

Brunet, C., Monié, P., Jolivet, L., Cadet, J.-P., 2000. Migration of compression and extension in the Tyrrhenian Sea, insights from $^{40}Ar/^{39}Ar$ ages on micas along a transect from Corsica to Tuscany. Tectonophysics 321, 127–155.

Cabassi, J., Venturi, S., Di Bennardo, F., Nisi, B., Tassi, F., Magi, F., Ricci, A., Picchi, G., Vaselli, O., 2021. Flux measurements of gaseous elemental mercury (GEM) from the geothermal area of “Le Biancane” natural park (Monterotondo Marittimo, Grosseto, Italy): Biogeochemical processes controlling GEM emission. Journal of Geochemical Exploration 228, 106824.

Caine, S.J., Forster, C.B. 1999. Fault zone architecture and fluid flow: insight from field data and numerical modeling. In: Haneberg, W.C., Mozley, P.S., Moore, J.C. & Goodwin, L.B. (eds) Faults and Subsurface Fluid Flow in the Shallow Crust. geophysical Monographs, American geophysical Union, 113, 101–127.

Caine, J.S., Evans, I.P., Forster, C.B., 1996. Fault zone architecture and permeability structure. Geology 24, 1025–1028.

Calcagnile, G., Panza, G.F., 1980. The main characteristics of the Lithosphere Asthenosphere System in Italy and surrounding regions. Pure Appl. Geophys. 119, 865–879.

Camarda, M., Gurrieri, S., Valenza, M., 2006. CO_2 flux measurements in volcanic areas using the dynamic concentration method: influence of soil permeability. J. Geophys. Res. 111, B05202.

Camarda, M., De Gregorio, S., Favara, R., Gurrieri, S., 2007. Evaluation of carbon isotope fractionation of soil CO2 under an advective–diffusive regimen: A tool for computing the isotopic composition of unfractionated deep source. Geochimica et Cosmochimica Acta, 71, 3016-3027.

Camarda, M., Gurrieri, S., Valenza, M., 2009. Effects of soil gas permeability and recirculation flux on soil CO_2 flux measurements performed using a closed dynamic accumulation chamber. Chemical Geology 265, 387-393.

Camarda, M., De Gregorio, S., Capasso, G., Di Martino, R.M.R., Gurrieri, S., Prano, V., 2019. The monitoring of natural soil CO_2 emissions: Issues and perspectives. Earth Sci. Rev. 198, 102928.

Cameli, G.M., Dini, I., Liotta, D., 1993. Upper crustal structure of the Larderello geothermal field as a feature of post collisional extensional tectonics (Southern Tuscany, Italy). Tectonophysics 224, 413–423.

Cameli, G.M., Dini, I., Liotta, D., 1998. Brittle/ductile boundary from seismic reflection lines of southern Tuscany (Northern Apennines, Italy). Mem. Soc. Geol. It. 52, 153–163.

Capasso, G., D'Alessandro, W., Favara, R., Inguaggiato, S., Parello, F., 2001. Kinetic isotope fractionation of CO_2 carbon due to diffusion processes through the soil. In: Cidu, R. (Ed.), Proc. 10th Internat Symp. Water-Rock Interaction, pp. 1497–1499.

Carapezza, M.L., Federico, C., 2000. The contribution of fluid geochemistry to the volcano monitoring of Stromboli. Journal of Volcanology and Geothermal Research, 95, 227-245.

Carapezza, M.L., Ranaldi, M., Gattuso, A., Pagliuca, N.M., Tarchini, L., 2015. The sealing capacity of the cap rock above the Torre Alfina geothermal reservoir (Central Italy) revealed by soil CO_2 flux investigations. Journal of Volcanology and Geothermal Research 291, 25–34.

Cardellini, C., Chiodini, G., Frondini, F., Avino, R., Bagnato, E., Caliro, S., Lelli, M., Rosiello, A., 2017. Monitoring diffuse volcanic degassing during volcanic unrests: the case of Campi Flegrei (Italy). Scientific Reports 7, 6757.

Carmignani, L., Decandia, F.A., Fantozzi, P.L., Lazzarotto, A., Liotta, D., Meccheri, M., 1994. Tertiary extensional tectonics in Tuscany (northern Apennines, Italy). Tectonophysics 238, 295–315.

Chiodini, G., Cioni, R., Guidi, M., Raco, B., Marini, L., 1998. Soil CO_2 flux measurements in volcanic and geothermal areas. Appl. Geochem., 13 (1998), pp. 543-552.

Chiodini, G., Avino, R., Brombach, T., Caliro, S., Cardellini, C., De Vita, S., Frondini, F., Granieri, D., Marotta, E., Ventura, G., 2004. Fumarolic and diffuse soil degassing west of Mount Epomeo, Ischia, Italy. Journal of Volcanology and Geothermal Research 133, 291–309.

Chiodini, G., Baldini, A., Barberi, F., Carapezza, M.L., Cardellini, C., Frondini, F., Granieri, D., Ranaldi, M., 2007. Carbon dioxide degassing at Latera caldera (Italy): geothermal reservoir and evaluation of its potential energy. Journal of Geophysical Research 112, 17.

Chiodini, G., Caliro, S., Cardellini, C., Avino, R., Granieri, D., Schmidt, A., 2008. Carbon isotopic composition of soil CO_2 efflux, a powerful method to discriminate different sources feeding soil CO_2 degassing in volcanic-hydrothermal areas. Earth and Planetary Science Letters 274, 372–379.

Chiodini, G., Cardellini, C., Lamberti, M.C., Agusto, M., Caselli, A., Liccioli, C., Tamburello, G., Tassi, F., Vaselli, O., Caliro, S., 2015. Carbon dioxide diffuse emission and thermal energy release from hydrothermal systems at Copahue–Caviahue Volcanic Complex (Argentina). Journal of Volcanology and Geothermal Research 304, 294–303.

Costantini, A., Lazzarotto, A., Liotta, D., Mazzanti, R., Mazzei, R., Salvatorini, G., 2002. Note Illustrative Della Carta Geologica d'Italia Alla Scala 1:50.000-Foglio 306 Massa Marittima. L.A.C. Firenze 172 pp.

Cox, S.F., Knackstedt, M.A., Braun, J., 2001. Principles of structural control on perme- ability and fluid flow in hydrothermal systems. Rev. Economic Geology 11, 1–24.

Curewitz, D., Karson, J.A., 1997. Structural settings of hydrothermal outflow: Fracture permeability maintained by fault propagation and interaction. Journal of Volcanology and Geothermal Research 79, 149-168.

David, M., 1977. Geostatistical Ore Reserve Estimation. Elsevier Science, New York, p. 384.

De Matteis, R., Vanorio, T., Zollo, A., Ciuffi, S., Fiordelisi, A., Spinelli, E., 2008. Three-dimensional tomography and rock properties of the Larderello-Travale geothermal area. Italy. Phys. Earth Plan. Int. 168, 37–48.

Della Vedova, B., Bellani, S., Pellis, G., Squarci, P., 2001. Deep temperatures and surface heat flow distribution. In: Vai, G.B., Martini, I.P. (Eds.), Anatomy of an Orogeny: the Apennines and Adjacent Mediterranean Basins. Kluwer Academic Publishers, Dordrecht, pp. 65–76.

Delsarte, I., Cohen, G.J.V., Momtbrun, M., Höhener, P., Atteia, O., 2021. Soil carbon dioxide fluxes to atmosphere: The role of rainfall to control CO_2 transport. Applied Geochemistry 127, 104854.

Dershowitz, W.S., Herda, H.H., 1992. Interpretation of fracture spacing and intensity. 33rd U.S. Symposium on Rock Mechanics (USRMS), Santa Fe, New Mexico, June 1992. Paper Number: ARMA-92-0757.

Di Stefano, R., Bianchi, I., Ciaccio, M.G., Carrara, G., Kissling, E., 2011. Three-dimensional Moho topography in Italy: new constraints from receiver functions and controlled source seismology. Geochemistry, Geophysics, Geosystems 12 (9), 1–15.

Dini, A., Gianelli, G., Puxeddu, M., Ruggieri, G., 2005. Origin and evolution of Pliocene–Pleistocene granites from the Larderello geothermal field (Tuscan Magmatic Province, Italy). Lithos 81, 1–31.

Dini, A., Westerman, D.S., Innocenti, F., Rocchi, S., 2008. Magma Emplacement in a Transfer Zone: the Miocene Mafic Orano Dyke Swarm of Elba Island 302. Geological Society London Special Publications, Tuscany, Italy, 131–148.

Duchi, V., Minissale, A.A., Rossi, R., 1986. Chemistry of thermal springs in the Larderello-Travale geothermal region, southern Tuscany, Italy. Applied Geochemistry 1, 659-667.

Duchi, V., Minissale, A.A., Manganelli, M., 1992. Chemical composition of natural deep and shallow hydrothermal fluids in the Larderello geothermal field. Journal of Volcanology and Geothermal Research 49, 313-328.

Elter, M., Pandeli, E., 1990. Alpine and Variscan orogenic phases in the basement rocks of the Northern Apennines (Larderello geothermal field, Southern Tuscany, Italy). Eclogae Geol. Helv. 83, 241–264.

Elter, P., Giglia, G., Tongiorgi, M., Trevisan, L., 1975. Tensional and compressional areas in the recent (Tortonian to Present) evolution on northern Apennines. Boll. Geofis. Teor. Appl. 65, 3–18.

Fariley, J.P., Hinds, J.J., 2004. Rapid transport pathways for geothermal fluids in an active Great Basin fault zone. Geology 32, 825–828.

Faulds, J.E., Coolbaugh, M.F., Hinz, N.H., Cashman, P.H., Kratt, C., Dering, G., Edwards, J., Mayhew, B., McLachlan, H., 2011. Assessment of favorable structural settings of geothermal systems in the Great Basin, western USA. Geothermal Resources Council Transactions 35, 777–784.

Faulkner, D.R., Jackson, C.A.L., Lunn, R.J., Schlische, R.W., Shipton, Z.K., Wibberley, C.A.J., Withjack, M.O., 2010. A review of recent developments concerning the structure, mechanisms and fluid flow properties of fault zones. J. Struct. Geol. 32, 1557–1575.

Federico, C., Corso, P.P., Fiordilino, E., Cardellini, C., Chiodini, G., Parello, F., Pisciotta, A., 2010. CO_2 degassing at La Solfatara volcano (Phlegrean Fields): Processes affecting $\delta^{13}C$ and $\delta^{18}O$ of soil CO_2. Geochimica et Cosmochimica Acta 74, 3521-3538.

Fischer, T.P., Aiuppa, A., 2020. AGU Centennial Grand Challenge: Volcanoes and Deep Carbon Global CO_2 Emissions From Subaerial Volcanism—Recent Progress and Future Challenges. Geochemistry, Geophysics, Geosystems 21, e2019GC008690.

Fisher, R. A., 1953. Dispersion on a sphere. Proceedings of the Royal Society of London. Series A. Mathematical and Physical Sciences, 217 (1130), 295-305

Fridriksson, T., Bjarni Reyr, K., Halld´or, A., Eygerður, M., Snj´olaug, ´O., Chiodini, G., 2006. CO_2 emissions and heat flow through soil, fumaroles, and steam heated mud pools at the Reykjanes geothermal area, SW Iceland. Applied Geochemistry 21 (9), 1551–91569.

Frondini, F., Caliro, S., Cardellini, C., Chiodini, G., Morgantini, N., 2009. Carbon dioxide degassing and thermal energy release in the Monte Amiata volcanic-geothermal area (Italy). Applied Geochemistry 24, 860–875.

Gherardi, F., Panichi, C., Gonfiantini, R., Magro, G., Scandiffio, G., 2005. Isotope systematics of C-bearing gas compounds in the geothermal fluids of Larderello, Italy. Geothermics 34, 442-470.

Giammanco, S., Melián, G., Neri, M., Hernández, P.A., Sortino, F., Barrancos, J., López, M., Pecoraino, G., Perez, N.M., 2016. Active tectonic features and structural dynamics of the summit area of Mt. Etna (Italy) revealed by soil CO_2 and soil temperature surveying. Journal of Volcanology and Geothermal Research 311, 79–98.

Gola, G., Bertini, G., Bonini, M. Botteghi, S., Brogi, A., De Franco, R., Dini, A., Donato, A., Gianelli, G., Liotta, D., Manzella, A., Montanari, D., Montegrossi, G., Petracchini, L., Ruggieri, G., Santilano, A., Scrocca, D., Trumpy, E., 2017. Data integration and conceptual modelling of the Larderello geothermal area, Italy. Energy Procedia, 125, 300–309.

Golder Associated Ltd., 2009. Derivation of Basic Fracture Properties. Golder Associates Ltd., Portland, USA.

Gudjónsdóttir, S.R., Ilyinskaya, E., Hreinsdóttir, S., Bergsson, B., Pfeffer, M.A., Michalczewska, K., Aiuppa, A., Óladóttir, A.A., 2020. Gas emissions and crustal deformation from the Krýsuvík high

temperature geothermal system, Iceland. Journal of Volcanology and Geothermal Research 391, 106350.

Harvey, M.C., Rowland, J.V., Chiodini, G., Rissmann, C., Bloomberg, S., Hernández, P.A., Mazot, A., Viveiros, F., Werner, C., 2015. Heat flux from magmatic hydrothermal systems related to availability of fluid recharge. Journal of Volcanology and Geothermal Research 302, 225–236.

Hernández, P.A., Pérez, N.M., Fridriksson, T., Jolie, E., Ilyinskaya, E., Thárhallsson, A., Ívarsson, G., Gíslason, G., Gunnarsson, I., Jónsson, B., Padrón, E., Melián, G., Mori, T., Notsu, K., 2012. Diffuse volcanic degassing and thermal energy release from Hengill volcanic system, Iceland. Bulletin of Volcanology 74, 2435–2448.

Hooker, P.J., Bertrami, R., Lombardi, S., O'Nions, R.K., Oxburgh, E.R., 1985. Helium-3 anomalies and crust-mantle interaction in Italy. Geochimica et Cosmochimica Acta 49, 2505-2513.

Jentsch, A., Jolie, E., Jones, D.G., Taylor-Curran, H., Peiffer, L., Zimmer, M., Lister, B., 2020. Magmatic volatiles to assess permeable volcano-tectonic structures in the Los Humeros geothermal field. Mexico. Journal of Volcanology and Geothermal Research 394, 106820.

Jentsch, A., Duesing, W., Jolie, E., Zimmer, M., 2021. Monitoring the response of volcanic CO_2 emission to changes in the Los Humeros hydrothermal system. Scientific Reports 11, 17972.

Jolie, E., Klinkmueller, M., Moeck, I., 2015. Diffuse surface emanations as indicator of structural permeability in fault-controlled geothermal systems. Journal of Volcanology and Geothermal Research 290, 97–113.

Jolie, E., Klinkmueller, M., Moeck, I., Bruhn, D., 2016. Linking gas fluxes at Earth's surface with fracture zones in an active geothermal field. Geology, 44 (3), 187–190, doi:10.1130/G37412.1

Kim, Y.S., Peacock, D.C.P., Sanderson, D.J., 2004. Fault damage zones. Journal of Structural Geology, 26, 503-517.

Klusman, R.W., Moore, J.N., LeRoy, M.P., 2000. Potential for surface gas flux measurements in exploration and surface evaluation of geothermal resources. Geothermics 29, 637-670.

Korneva, I., Cilona, A., Tondi, E., Agosta, F., Giorgioni, M., 2015. Characterisation of the permeability anisotropy of Cretaceous platform carbonates by using 3D fracture modeling: the case study of Agri Valley fault zones (southern Italy). Ital. J. Geosci., Vol. 134, No. 3, 396-408.

Krige, D.G., 1951. A statistical approach to some basic mine valuation problems on the Witwatersrand. Journal of the Southern African Institute of Mining and Metallurgy 52, 119–139.

Lamberti, M.C., Vigide, N., Venturi, S., Agusto, M., Yagupsky, D., Winocur, D., Barcelona, H., Velez, M.L., Cardellini, C., Tassi, F., 2019. Structural architecture releasing deep-sourced carbon dioxide diffuse degassing at the Caviahue–Copahue Volcanic Complex. Journal of Volcanology and Geothermal Research 374, 131–141.

Lamberti, M.C., Chiodi, A., Agusto, M., Filipovich, R., Massenzio, A., Báez, W., Tassi, F., Vaselli, O., 2021. Carbon dioxide diffuse degassing as a tool for computing the thermal energy release at

Cerro Blanco Geothermal System, Southern Puna (NW Argentina). Journal of South American Earth Sciences 105, 102833.

Lazzarotto, A., 1967. Geologia della zona compresa fra l'alta valle del Fiume Cornia ed il torrente Pavone (provincia di Pisa e Grosseto). Mem. Soc. Geol. Ital. 6, 151–197.

Lazzarotto, A., Mazzanti, R., 1978. Geologia dell'alta Val Di Cecina. Boll. Soc. Geol. Ital. 95, 1365–1487.

Leila, M., Lévy, D., Battani, A., Piccardi, L., Šegvić, B., Badurina, L., Pasquet, G., Combaudon, V., Moretti, I., 2021. Origin of continuous hydrogen flux in gas manifestations at the Larderello geothermal field, Central Italy. Chemical Geology 585, 120564.

Lelli, M., Raco, B., 2017. A reliable and effective methodology to monitor CO_2 flux from soil: The case of Lipari Island (Sicily, Italy). Applied Geochemistry 85, 73–85.

Lewicki, J.L., Bergfeld, D., Cardellini, C., Chiodini, G., Granieri, D., Varley, N., Werner, C., 2005. Comparative soil CO_2 flux measurements and geostatistical estimation methods on Masaya volcano, Nicaragua. Bulletin of Volcanology 68, 76-90.

Lewicki, J.L., Hilley, G.E., 2009. Eddy covariance mapping and quantification of surface CO_2 leakage fluxes. Geophysical Research Letters 36, L21802.

Liotta, D., 1991. The Arbia-Val Marecchia Line, Northern Apennines. Eclogae Geol. Helv. 84, 413–430.

Liotta, D., Brogi, A., 2020. Pliocene-Quaternary fault kinematics in the Larderello geo- thermal area (Italy): Insights for the interpretation of the present stress field. Geothermics 83, 101714.

Liotta, D., Ranalli, G., 1999. Correlation between seismic reflectivity and rheology in extended lithosphere: southern Tuscany, Inner Northern Apennines, Italy. Tectonophysics 315, 109–122.

Liotta, D., Cernobori, L., Nicolich, R., 1998. Restricted rifting and its coexistence with compressional structures: results from the Crop03 traverse (Northern Apennines, Italy). Terra Nova 10, 16–20.

Locardi, E., Nicolich, R., 1988. Geodinamica del Tirreno e dell'Appennino centro-meridionale: la nuova carta della Moho. Mem. Soc. Geol. Ital., 41, 121-140

Lubenow, B.L., Fairely, J.P., Lindsey, C.R., Larson, P.B., 2016. Influences on shallow ground temperatures in high flux thermal systems. Journal of Volcanology and Geothermal Research 323, 53-61.

Lucia, F.J., 1999. Carbonate Reservoir Characterization. Springer-Verlag, New York, USA. 336 pp.

Magro, G., Ruggieri, G., Gianelli, G., Bellani, S., 2003. Helium isotopes in paleofluids and present-day fluids of the Larderello geothermal field: Constraints on the heat source. Journal Of Geophysical Research 108, B1.

Manzella, A., Bonciani, R., Allansdottir, A., Botteghi, S., Donato, A., Giamberini, S., Lenzi, A., Paci, M., Pellizzone, A., Scrocca, D., 2018. Environmental and social aspects of geothermal energy in Italy. Geothermics 72, 232-248.

Martini, I.P., Sagri, M., 1993. Tectono-sedimentary characteristics and the genesis of the recent magmatism of Southern Tuscany and Northern Latium. Per. Mineral. 56, 157–172.

Martini, I., Ambrosetti, E., Brogi, A., Aldinucci, M., Zwaan, F., Sandrelli, F., 2021. Polyphase extensional basins: interplay between tectonics and sedimentation in the Neogene Siena-Radicofani Basin (Northern Apennines, Italy). International Journal of Earth Sciences 110(5), 1729–1751. 10.1007/s00531-021-02038-4.

Mason, E., Edmonds, M., Turchyn, A.V., 2017. Remobilization of crustal carbon may dominate volcanic arc emissions. Science 357, 290–294.

Matheron, G., 1970. The theory of regionalized variables and its applications. Fascicule n. 5, Les Cahiers du Centre De Morphologie Mathématique, Ecole des Mines de Paris, Fontainebleau 211.

Minissale, A., 1991. The Larderello geothermal field: a review. Earth Sciences Reviews, 31. 133-151.

Minissale, A., Evans, W.C., Magro, G., Vaselli, O., 1997. Multiple source components in gas manifestations from north-central Italy. Chemical Geology 142, 175-192.

Moeller, S., Grevemeyer, I., Ranero, C. R., Berndt, C., Klaeschen, D., Sallarès, V., Zitellini, N., de Franco, R., 2013. Early-stage rifting of the northern Tyrrhe- nian Sea Basin: Results from a combined wide-angle and multichannel seismic study. Geochemistry, Geophysics, Geosystems, 14(8), 3032–3052. https://doi.org/10.1002/ggge.20180

Molli, G., 2008. Northern Apennine–Corsica orogenic system: an updated overview. Geological Society, London, Special Publications 298, 413–442.

Nelson, R.A., 2001. Geologic Analysis of Naturally Fractured Reservoirs. Gulf Professional Publishing, 332 pp.

Nisi, B., Vaselli, O., Marchev, P., Tassi, F., 2013. Diffuse CO_2 soil flux measurements at the youngest volcanic system in Bulgaria: the 12.2 Ma old Kozhuh cryptodome. Acta Vulcanologica 25, 169–178.

Nisi, B., Vaselli, O., Tassi, F., Elio, J., Ortega, M., Caballero, J., Rappuoli, D., Mazadiego, L.F., 2014. Origin of the gases released from the Acqua Passante and Ermeta wells (Mt. Amiata, central Italy) and possible environmental implications for their closure. Annals of Geophysics, 57, S0438.

Oda, M., 1985. Permeability tensor for discontinuous rock masses. Géotechnique, vol. 35 (4), 483-495.

Orlandi, P., 2006. Siti di interesse minerario e mineralogico della Provincia di Pisa. Piano Territoriale di Coordinamento Approvato con Deliberazione di Consiglio Provinciale n. 100 del 27/07/2006. (In Italian).

Pandeli, E., Bertini, G., Castellucci, P., 1991. The tectonic wedges complex of the Larderello area (southern Tuscany, Italy). Boll. Soc. Geol. Ital. 110, 621–629.

Pandeli, E., Gianelli, G., Puxeddu, M., Elter, F.M., 1994. The paleozoic basement of the northern Apennines: stratigraphy, tectono-metamorphic evolution and alpine hydrothermal processes. Mem. Soc. Geol. Ital. 48, 627–654.

Parkinson K. J., 1981. An improved method for measuring soil respiration in the field. Journal of Applied Ecology 18, 221-228.

Pauselli, C., Gola, G., Mancinelli, P., Trumpy, E., Saccone, M., Manzella, A., and Ranalli, G., 2019, A new surface heat flow map of the Northern Apennines between latitudes 42.5 and 44.5 N. Geothermics 81, p. 39–52.

Peiffer, L., Carrasco-Núñez, G., Mazot, A., Villanueva-Estrada, R.E., Inguaggiato, C., Bernard-Romero, R., Rocha Miller, R., Rojas, J.H., 2018. Soil degassing at the Los Humeros geothermal field (Mexico). Journal of Volcanology and Geothermal Research 356, 163–174.

Pérez, N.M., Padilla, G.D., Padrón, E., Hernández, P.A., Melián, G.V., Barrancos, J., Dionis, S., Nolasco, D., Rodríguez, F., Calvo, D., Hernández, I., 2012. Precursory diffuse CO_2 and H_2S emission signatures of the 2011–2012 El Hierro submarine eruption, Canary Islands. Geophys. Res. Lett. 39, L16311.

Queißer, M., Burton, M., Kazahaya, R., 2019. Insights into geological processes with CO_2 remote sensing – a review of technology and applications. Earth Sci. Rev. 188, 389–426. https://doi.org/10.1016/j.earscirev.2018.11.016.

Raich, J.W., Schlesinger, W.H., 1992. The global carbon dioxide flux in soil respiration and its relationship to vegetation and climate. Tellus 44B, 81–99.

Regione Toscana, 2014. Supplemento al Bollettino Ufficiale della Regione Toscana n. 13 del 2.4.2014. Allegato A. (In Italian).

Rissmann, C., Christenson, B., Werner, C., Leybourne, M., Cole, J., Gravley, D., 2012. Surface heat flow and CO_2 emissions within the Ohaaki hydrothermal field, Taupo Volcanic Zone, New Zealand. Applied Geochemistry 27, 223–239.

Rochira, F., Caggianelli, A., De Lorenzo, S., 2018. Regional thermo-rheological field related to granite emplacement in the upper crust: Implications for the Larderello area (Tuscany, Italy). Geodinamic Acta, 30, 225–240.

Rolleau, E., Bravo, F., Pinti, D.L., Barde-Cabusson, S., Pizarro, M., Tardani, D., Muñoz, C., Sanchez, J., Sano, Y., Takahata, N., de la Cal, F., Esteban, C., Morata, D., 2017. Structural controls on fluid circulation at the Caviahue-Copahue Volcanic Complex (CCVC) geothermal area (Chile-Argentina), revealed by soil CO_2 and temperature, self-potential, and helium isotopes. Journal of Volcanology and Geothermal Research 341, 104–118.

Romagnoli, P., Arias, A., Barelli, A., Cei, M., Casini, M., 2010. An updated numerical model of the Larderello–Travale geothermal system, Italy. Geothermics 39, 292–313.

Rossetti, F., Faccenna, C., Jolivet, L., Goffé, B., Funiciello, R., 2002. Structural signature and exhumation P-T-t paths of the blueschist units exposed in the interior of the Northern Apennine chain, tectonic implications. Boll. Soc. Geol. Ital. 1, 829–842.

Rowland, J.V., Sibson, R.H., 2004. Structural controls on hydrothermal flow in a segmented rift system Taupo Volcanic Zone, New Zealand. Geofluids 4, 259–283.

Sbrana, A., Marianelli, P., Belgiorno, M., Sbrana, M., Ciani, V., 2020. Natural CO_2 degassing in the Mount Amiata volcanic–geothermal area. Journal of Volcanology and Geothermal Research 397, 106852.

Scandiffio, G., Panichi, C., Valenti, M., 1995. Geochemical evolution of fluids in the Larderello geothermal field. In: Proceedings of the Geothermal Congress 1995, 18–31 May, Florence, Italy (E. Barbier et al. eds.), 1839-1843.

Serri, G., Innocenti, F., Manetti, P., 2001. Magmatism from Mesozoic to Present: petrogenesis, time-space distribution and geodynamic implications. In: Vai, G.B., Martini, I.P. (Eds.), Anatomy of an Orogen: The Apennines and Adjacent Mediterranean Basins. Kluwer Academic Publishers, Amsterdam, pp. 77–103.

Serri, G., Innocenti, F., Manetti, P., 1993. Geochemical and petrological evidence of the subduction of delaminated Adriatic continental lithosphere in the genesis of the Neogene-Quaternary magmatism of central Italy. Tectonophysics 223, 117–214.

Sharp, Z.D., 2017. Principles of Stable Isotope Geochemistry. 2nd edition.

Sibson, R.H., 2000. Fluid involvement in normal faulting. In: In: Cello, G., Tondi, E. (Eds.), The Resolution of Geological Analysis and Models for Earthquake Faulting Studies J. Geodynam. 29, 469–499.

Silvestri, M., Marotta, E., Buongiorno, M.F., Avvisati, G., Belviso, P., Bellucci Sessa, E., Caputo, T., Longo, V., De Leo, V., Teggi, S., 2020. Monitoring of Surface Temperature on Parco delle Biancane (Italian Geothermal Area) Using Optical Satellite Data, UAV and Field Campaigns. Remote Sensing 12, 2018.

Sinclair, A.J., 1974. Selection of threshold values in geochemical data using probability graphs. Journal of Geochemical Exploration 3, 129–149.

Snow, D. T., 1965. A parallel plate model of fractured permeable media. University of California, Berkeley.

Spiess, R., Langone, A., Caggianelli, A., Stuart, F.M., Zucchi, M., Bianco, C., Brogi, A., Liotta, D., 2021. Unveiling ductile deformation during fast exhumation of a granitic pluton in a transfer zone. Journal of Structural Geology 147, 104326.

Tassi, F., Fiebig, J., Vaselli, O., Nocentini, M., 2012. Origins of methane discharging from volcanic-hydrothermal, geothermal and cold emissions in Italy. Chemical Geology 310–311, 36–48.

Tassi, F., Nisi, B., Cardellini, C., Capecchiacci, F., Donnini, M., Vaselli, O., Chiodini, G., 2013. Diffuse soil emission of hydrothermal gases (CO_2, CH_4, and C_6H_6) at Solfatara crater (Campi Flegrei, southern Italy). Applied Geochemistry 35, 142–153.

Tassi, F., Cabassi, J., Calabrese, S., Nisi, B., Venturi, S., Capecchiacci, F., Giannini, L., Vaselli, O., 2016. Diffuse soil gas emissions of gaseous elemental mercury (GEM) from hydrothermal-volcanic systems: an innovative approach by using the static closed-chamber method. Applied Geochemistry, 66, 234–241.

Taussi, M., Nisi, B., Pizarro, M., Morata, D., Veloso, E.A., Volpi, G., Vaselli, O., Renzulli, A., 2019. Sealing capacity of clay-cap units above the Cerro Pabellón hidden geothermal system (northern Chile) derived by soil CO_2 flux and temperature measurements. Journal of Volcanology and Geothermal Research 384, 1–14.

Taussi, M., Nisi, B., Vaselli, O., Maza, S., Morata, D., Renzulli, A., 2021. Soil CO_2 and temperature from a new geothermal area in the Cordón de Inacaliri Volcanic Complex (Northen Chile). Geothermics 89, 101961.

Terzaghi, R., 1965. Sources of Error in Joint Surveys. Géotechnique, 15, 287-304.

Theye, T., Reinhardt, J., Goffé, B., Jolivet, L., & Brunet, C., 1997. Ferro-and magnesiocarpholite from the Monte Argentario (Italy): First evidence for high-pressure metamorphism of the metasedimentary Verrucano sequence, and significance for PT path reconstruction. European Journal of Mineralogy, 859-874.

Vai, G.B., Martini, I.P., 2001. Anatomy of an Orogen: the Apennines and Adjacent Mediterranean Basins. Kluwer Academic, Dordrecht, 2001.

Venturi, S., Tassi, F., Bicocchi, G., Cabassi, J., Capecchiacci, F., Capasso, G., Vaselli, O., Ricci, A., Grassa, F., 2017. Fractionation processes affecting the stable carbon isotope signature of thermal waters from hydrothermal/volcanic systems: The examples of Campi Flegrei and Vulcano Island (southern Italy). Journal of Volcanology and Geothermal Research 345, 46–57.

Venturi, S., Tassi, F., Magi, F., Cabassi, J., Ricci, A., Capecchiacci, F., Caponi, C., Nisi, B., Vaselli, O., 2019. Carbon isotopic signature of interstitial soil gases reveals the potential role of ecosystems in mitigating geogenic greenhouse gas emissions: case studies from hydrothermal systems in Italy. Science of the Total Environment 655, 887–898.

Viveiros, F., Cardellini, C., Ferreira, T., Caliro, S., Chiodini, G., Silva, C., 2010. Soil CO_2 emissions at Furnas volcano, São Miguel Island, Azores archipelago: Volcano monitoring perspectives, geomorphologic studies, and land use planning application. Journal of Geophysical Research 115, B12208.

Viveiros, F., Chiodini, G., Cardellini, C., Caliro, S., Zanon, V., Silva, C., Rizzo, A.L., Hipólito, A., Moreno, L., 2020. Deep CO_2 emitted at Furnas do Enxofre geothermal area (Terceira Island, Azores archipelago). An approach for determining CO_2 sources and total emissions using carbon isotopic data. Journal of Volcanology and Geothermal Research 401, 106968.

Werner, C., Cardellini, C., 2006. Comparison of carbon dioxide emissions with fluid upflow, chemistry, and geologic structures at the Rotorua geothermal system, New Zealand. Geothermics 35, 221–238.

Werner, C., Bergfeld, D., Farrar, C.D., Doukas, M.P., Kelly, P.J., Kern, C., 2016. Decadal-scale variability of diffuse CO_2 emissions and seismicity revealed from long-term monitoring (1995–2013) at Mammoth Mountain, California, USA. Journal of Volcanology and Geothermal Research 289, 1, 51-63

Whiticar, M.J., 1999. Carbon and hydrogen isotope systematics of bacterial formation and oxidation of methane. Chemical Geology 161, 291–314.

Zambrano, M., Tondi, E., Korneva, I., Panza, E., Agosta, F., Janiseck, J. M., Giorgioni, M., 2016. Fracture properties analysis and discrete fracture network modelling of faulted tight limestones, Murge Plateau, Italy. Italian Journal of Geosciences, 135(1), 55-67.

Zucchi, M., Brogi, A., Liotta, D., Rimondi, V., Ruggieri, G., Montegrossi, G., Caggianelli, A., Dini, A., 2017. Permeability and hydraulic conductivity of faulted micaschist in the eastern Elba Island exhumed geothermal system (Tyrrhenian sea, Italy): insights from Cala Stagnone. Geothermics 70, 125–145.

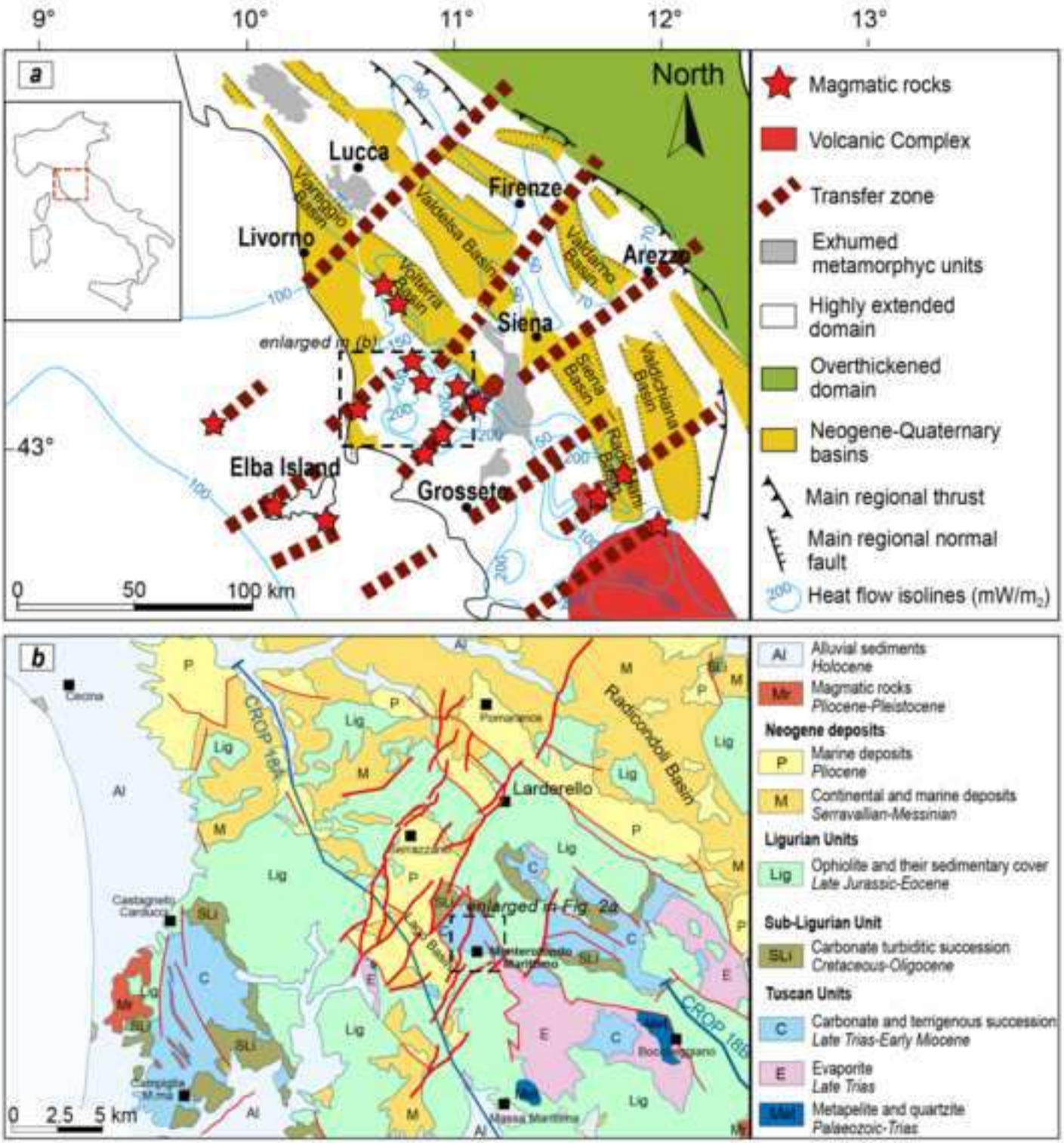

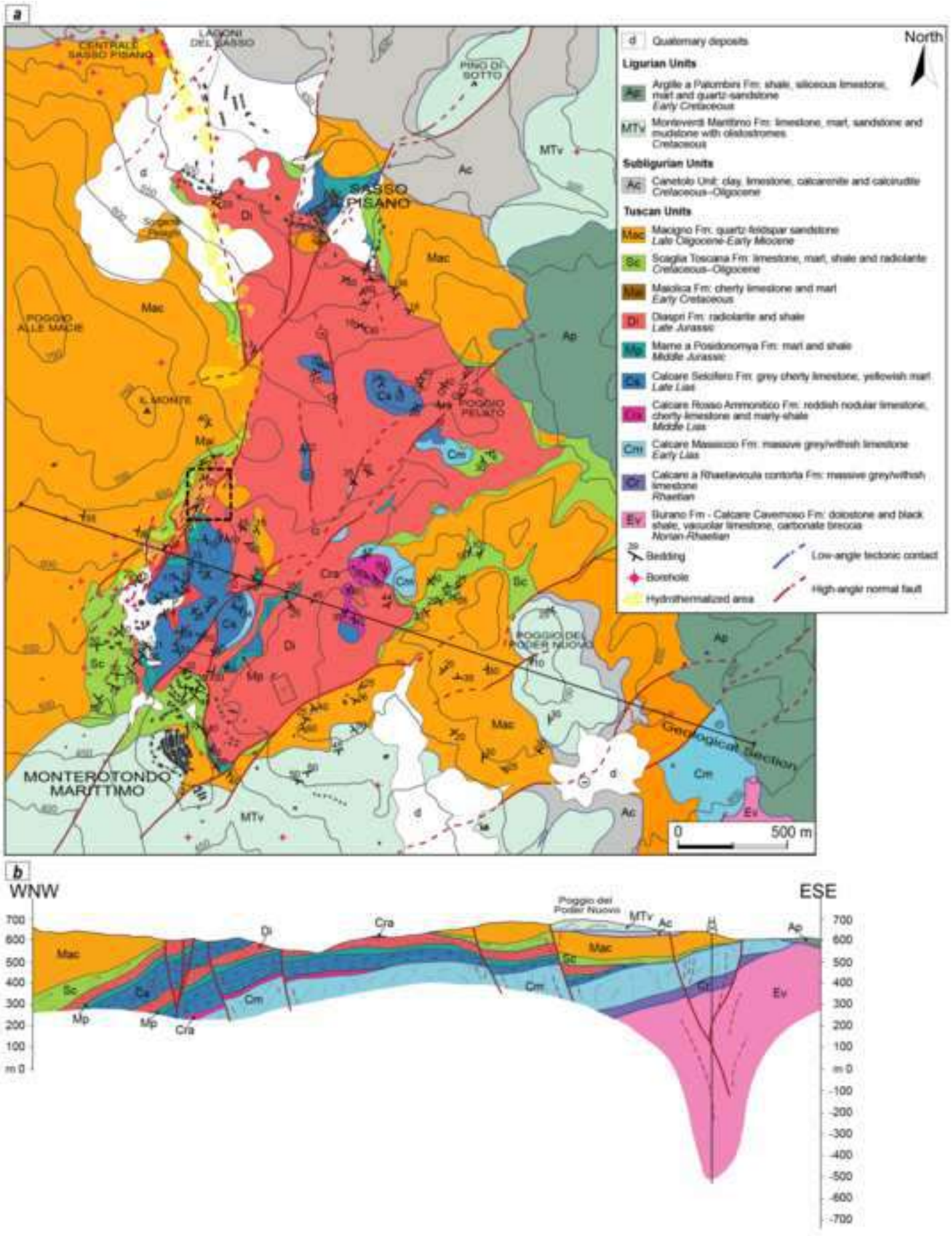

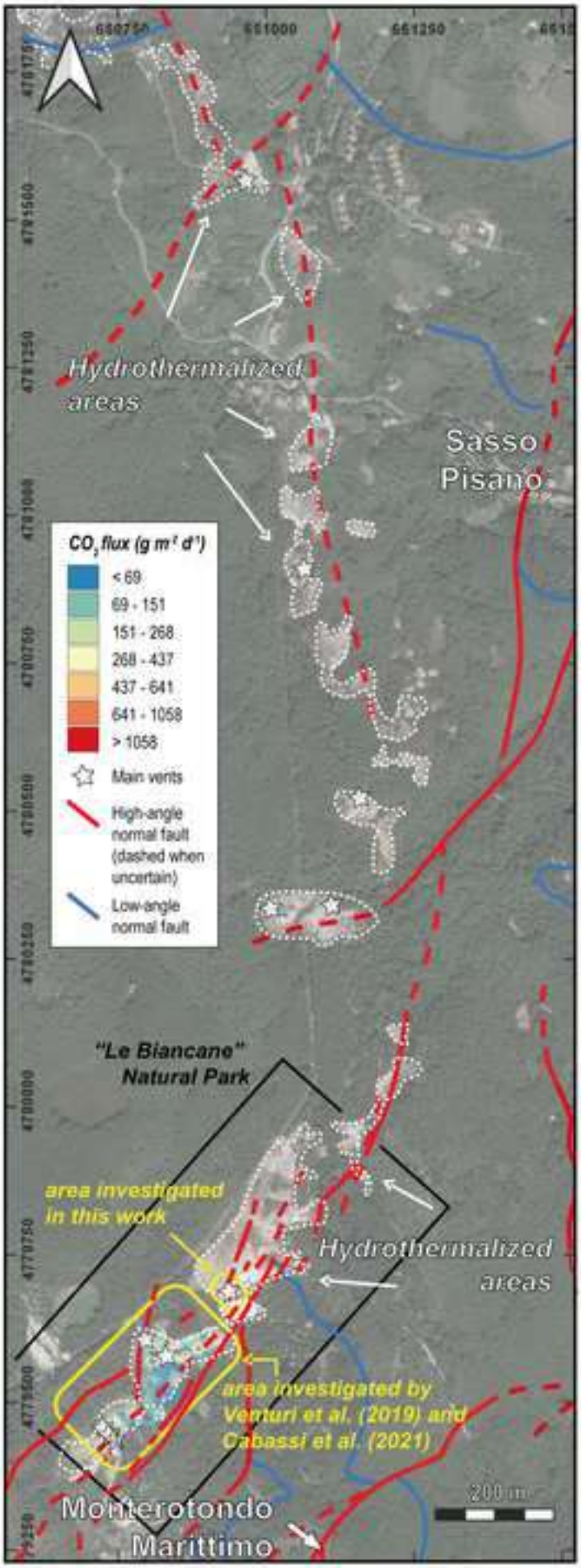

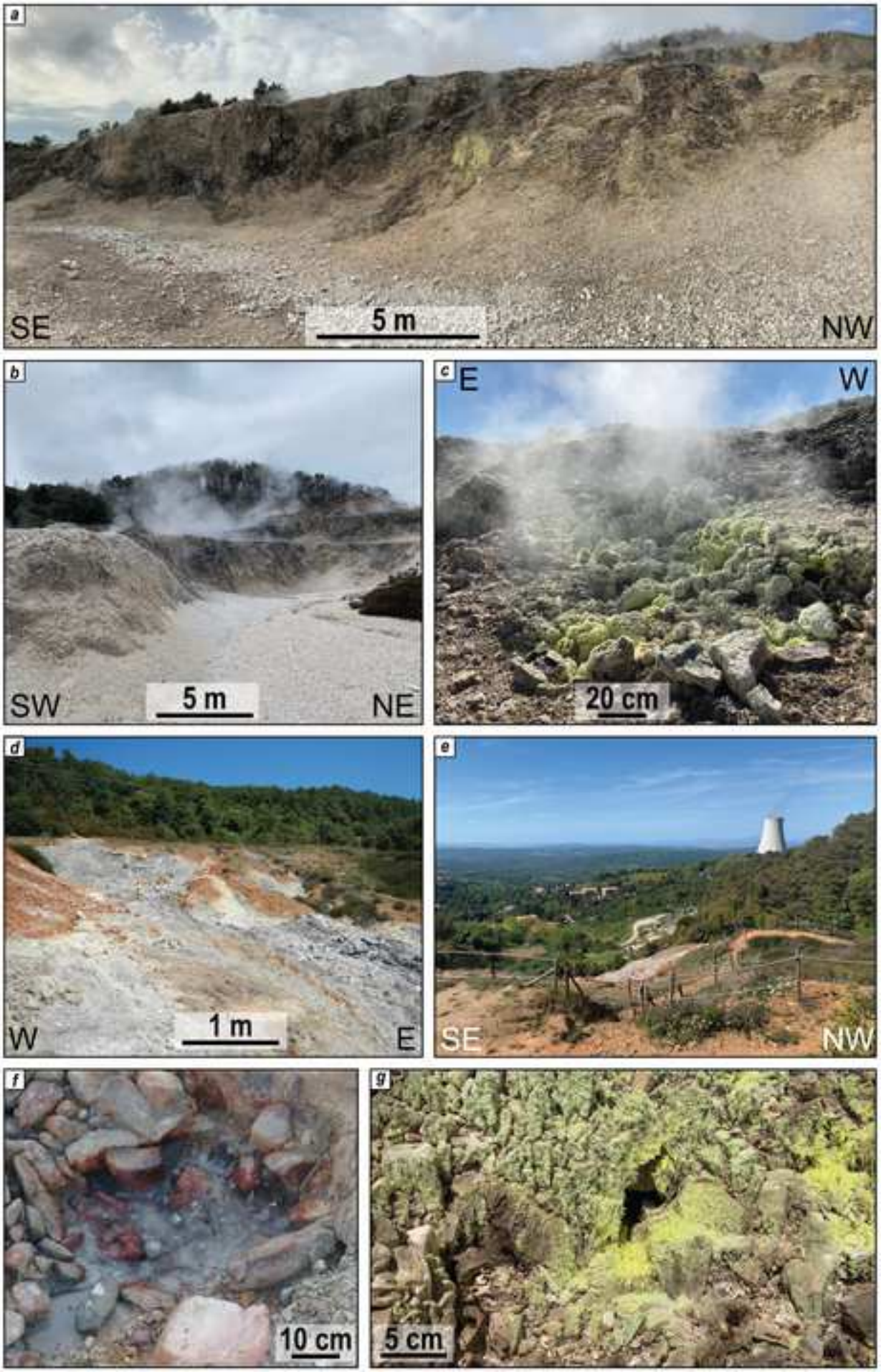

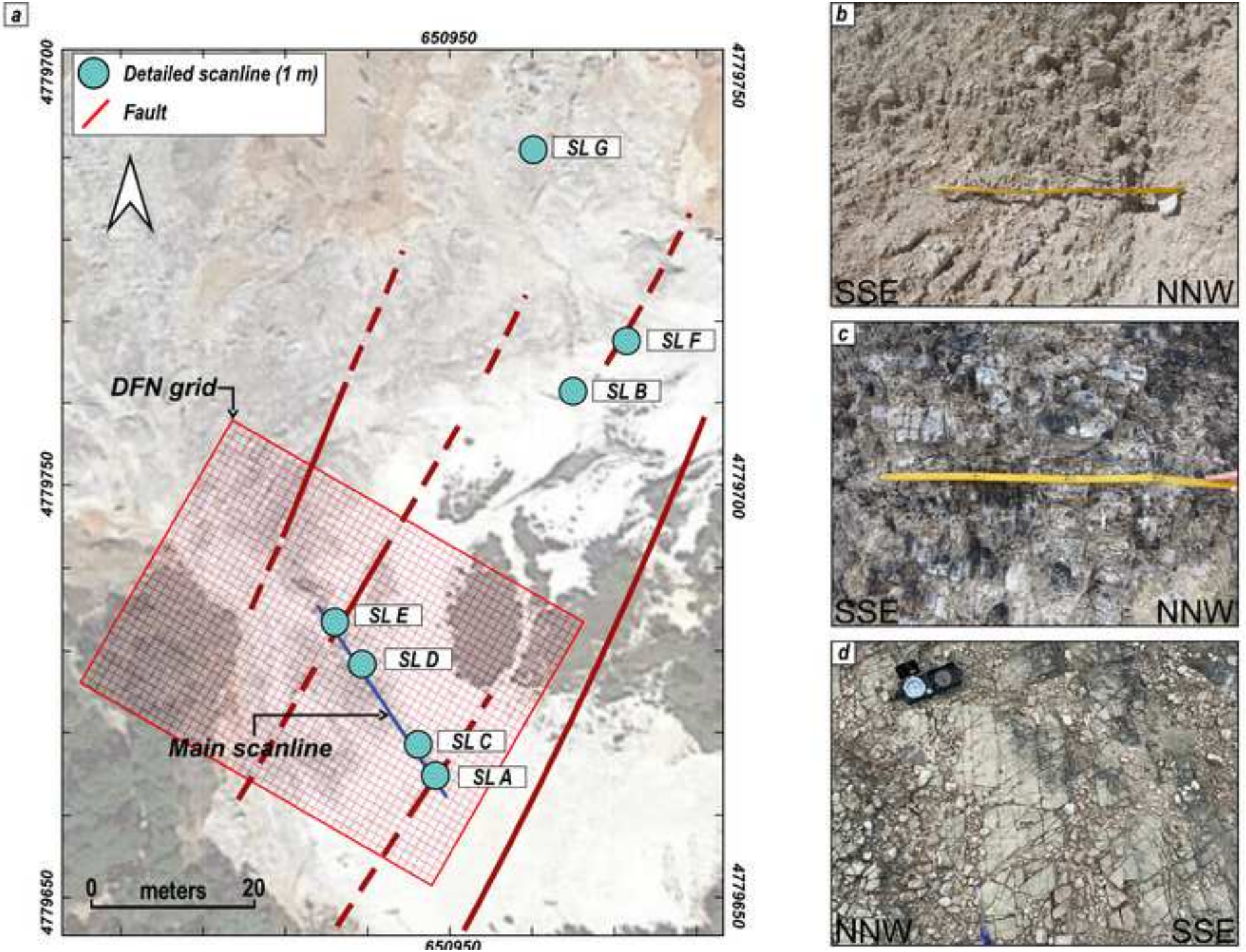

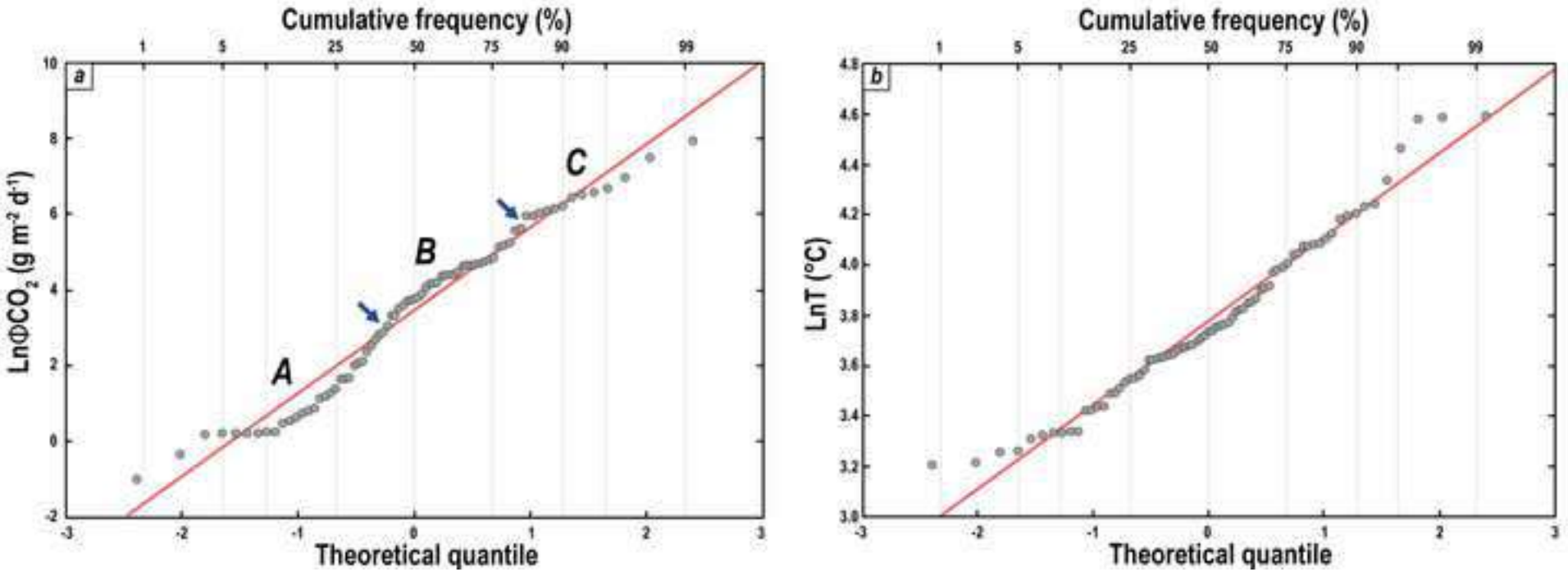

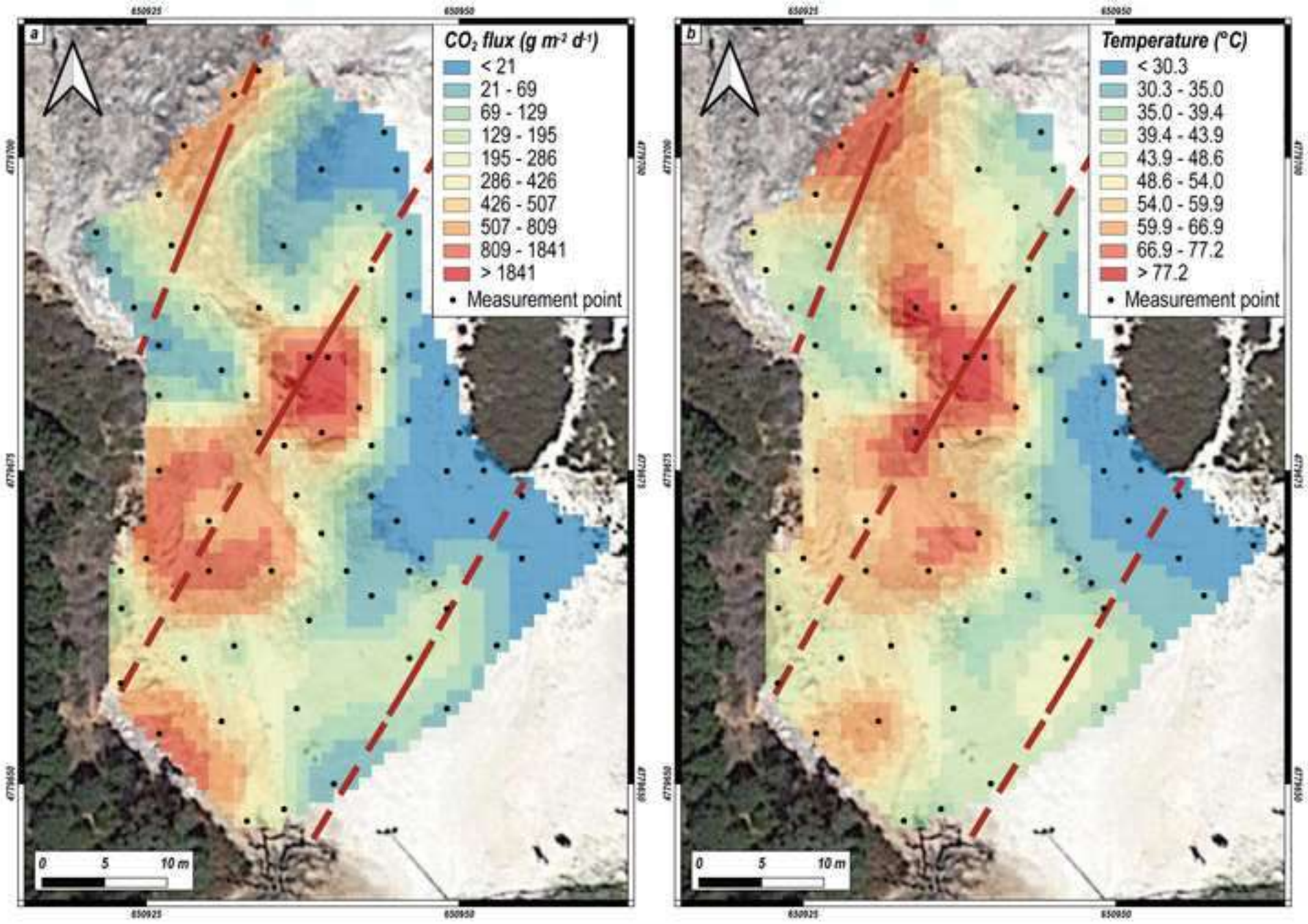

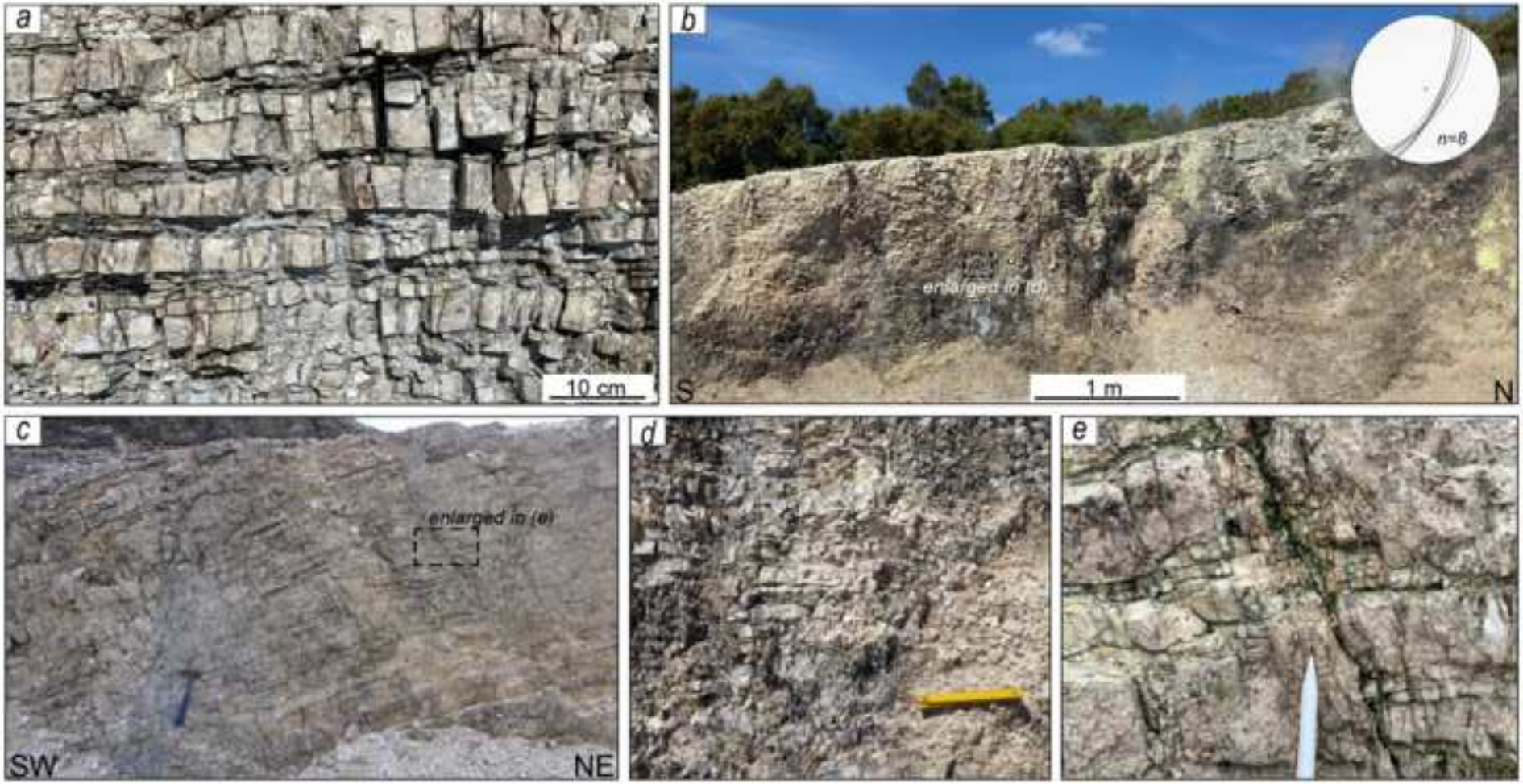

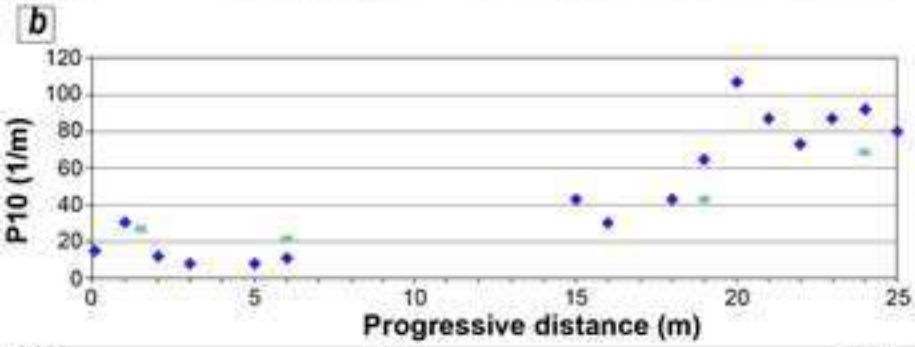

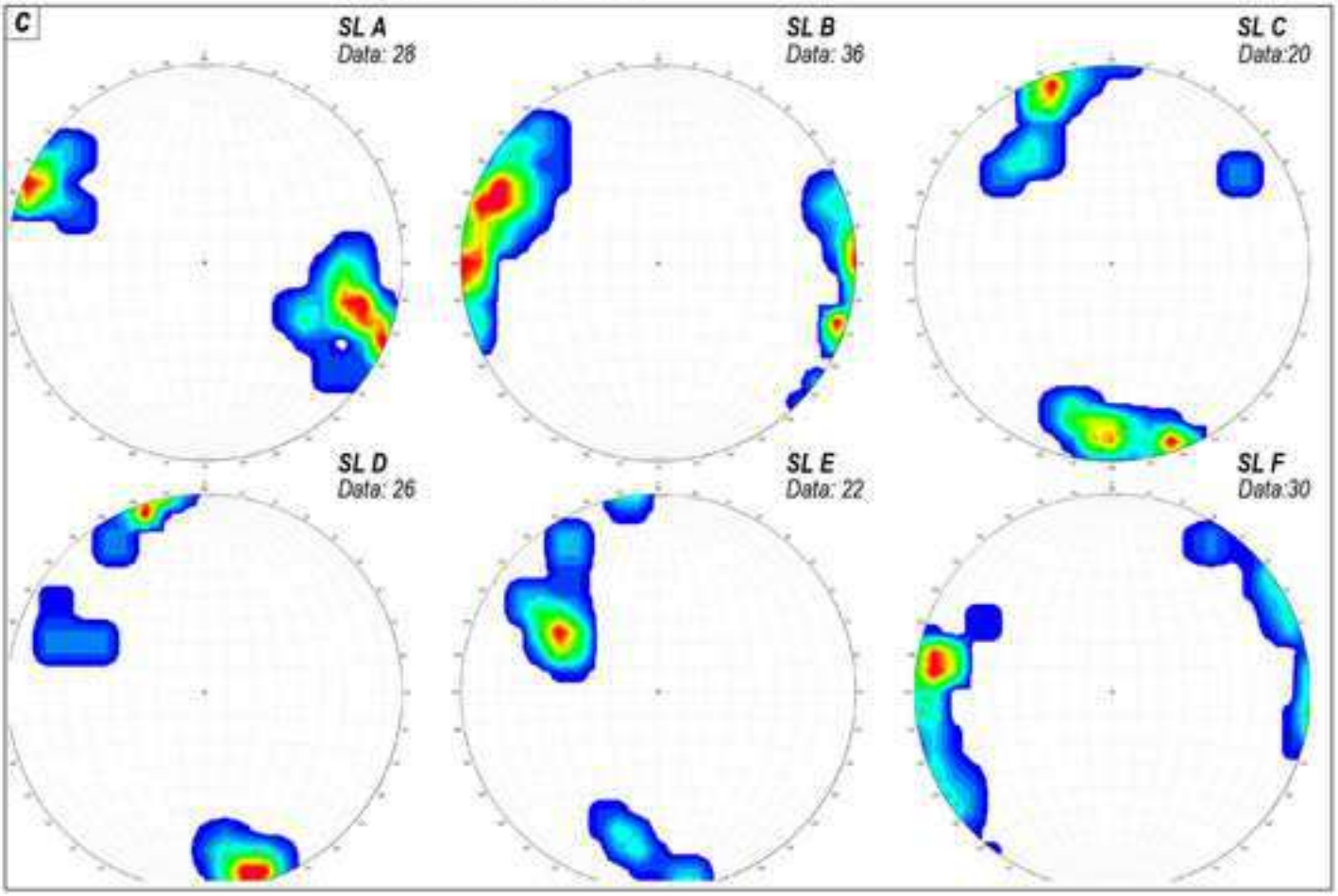

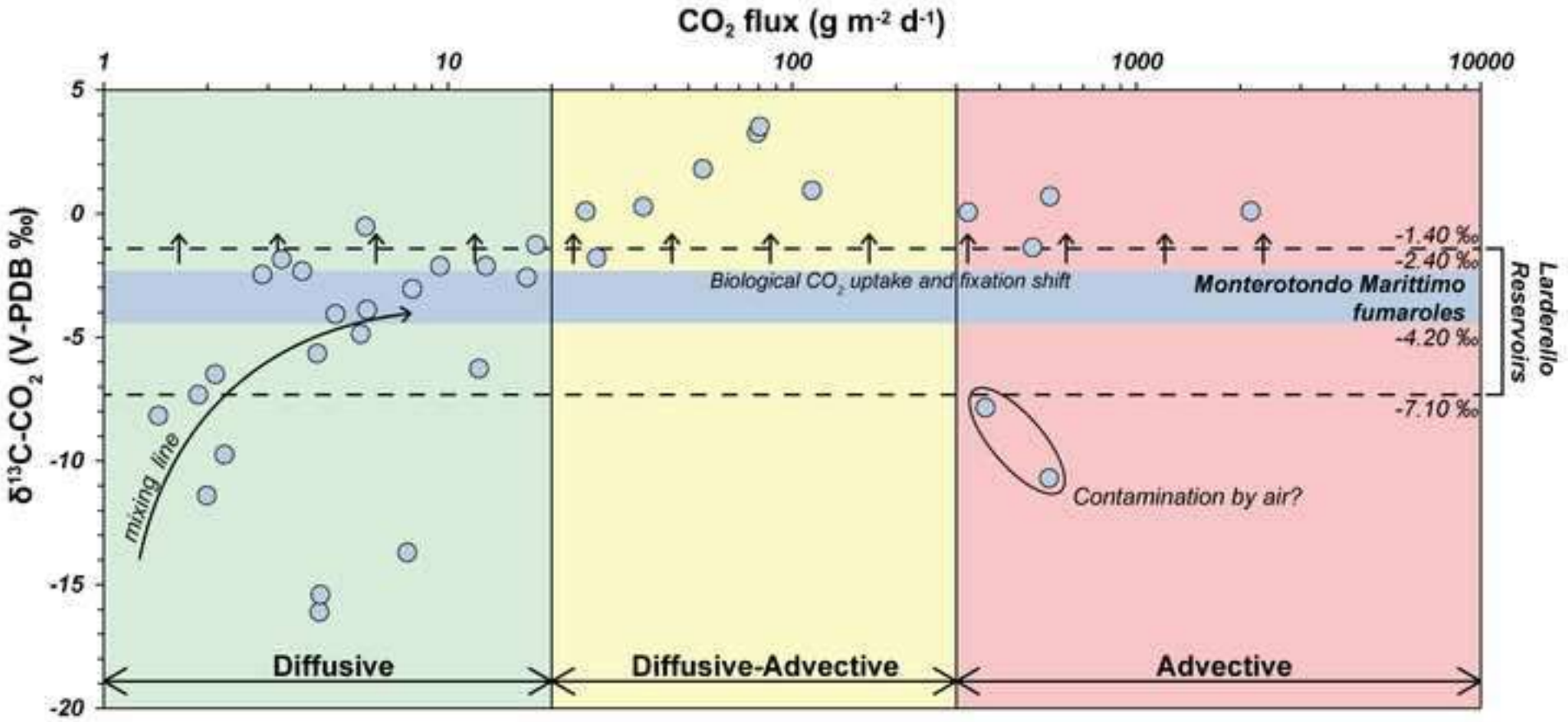

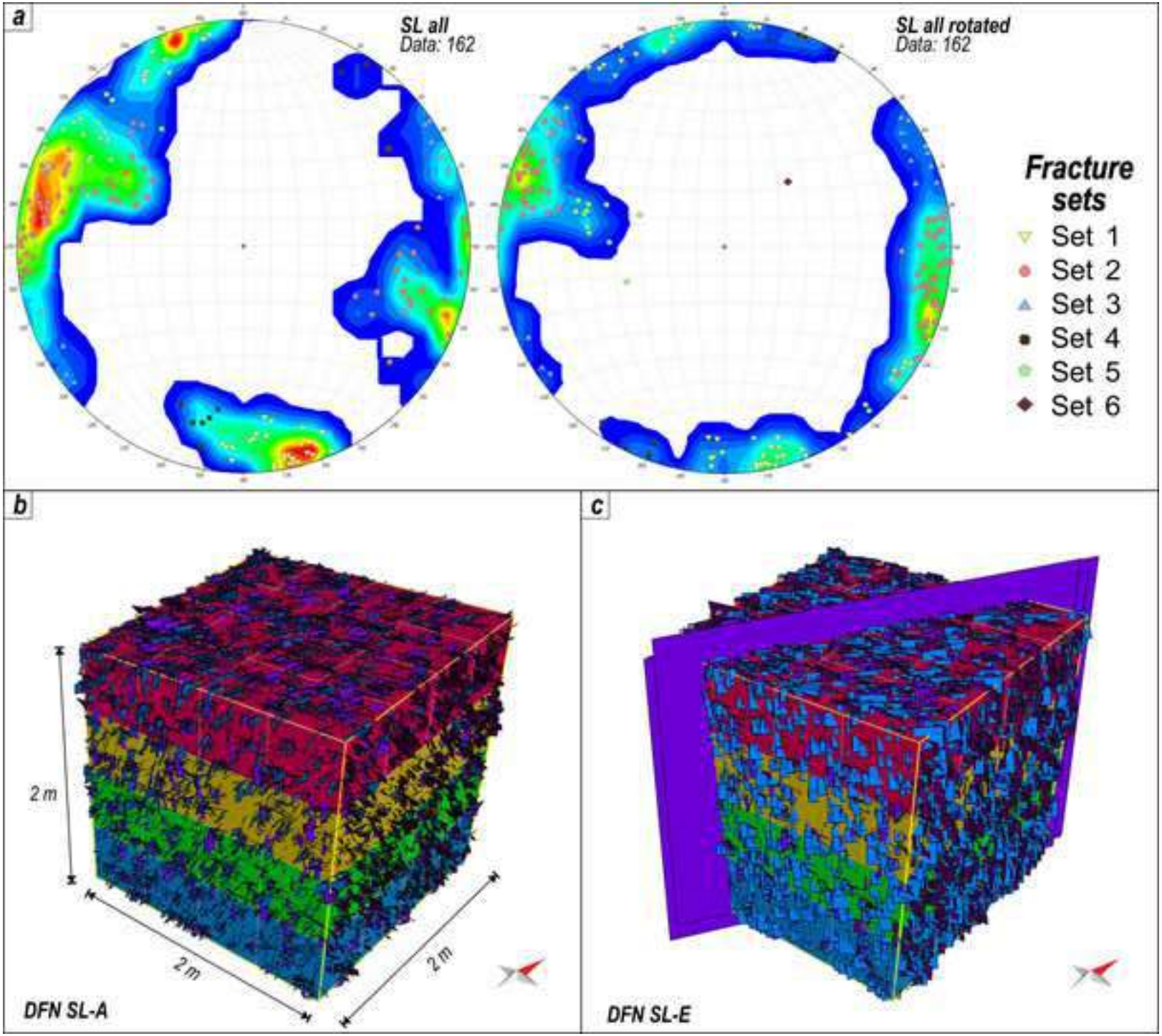

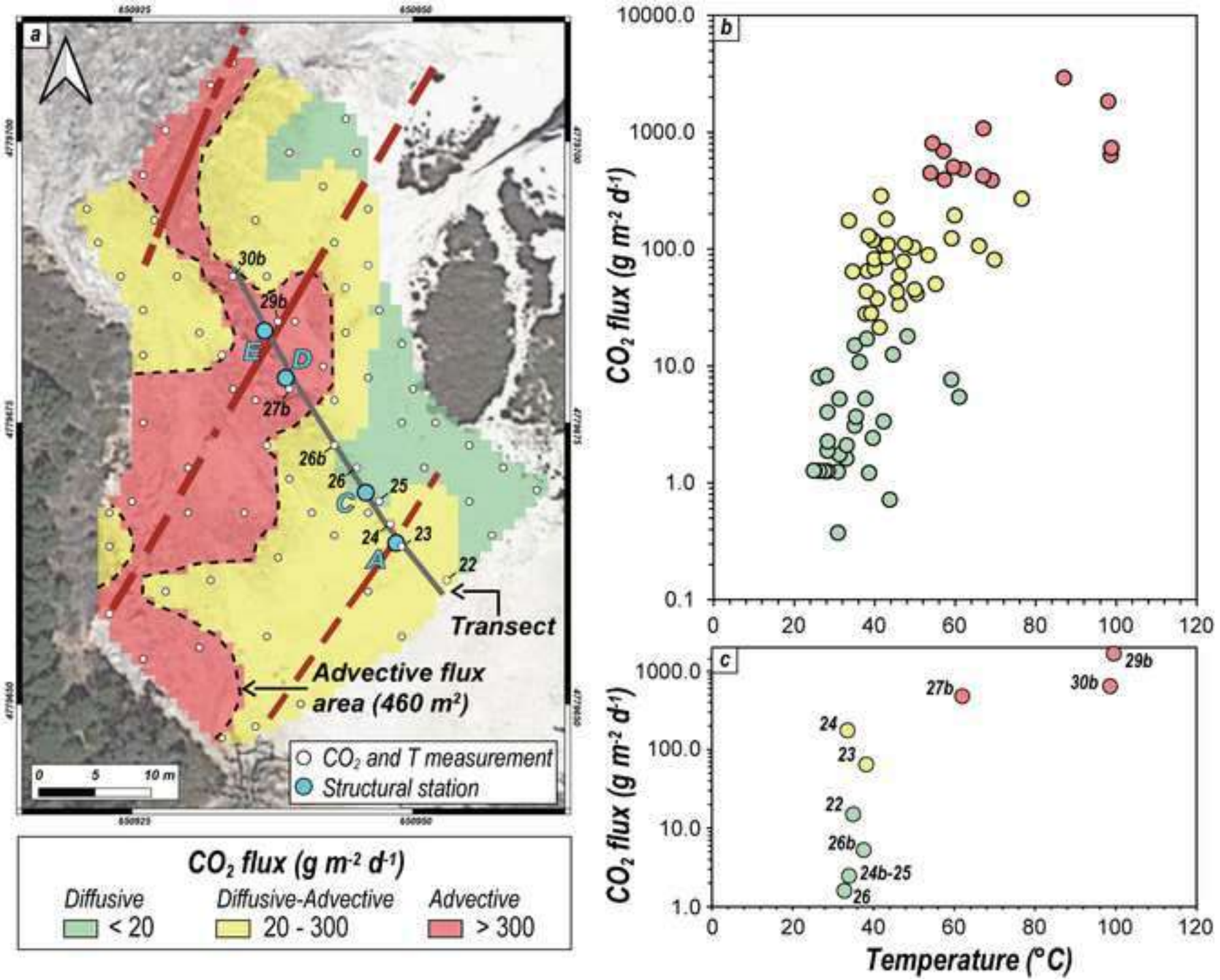

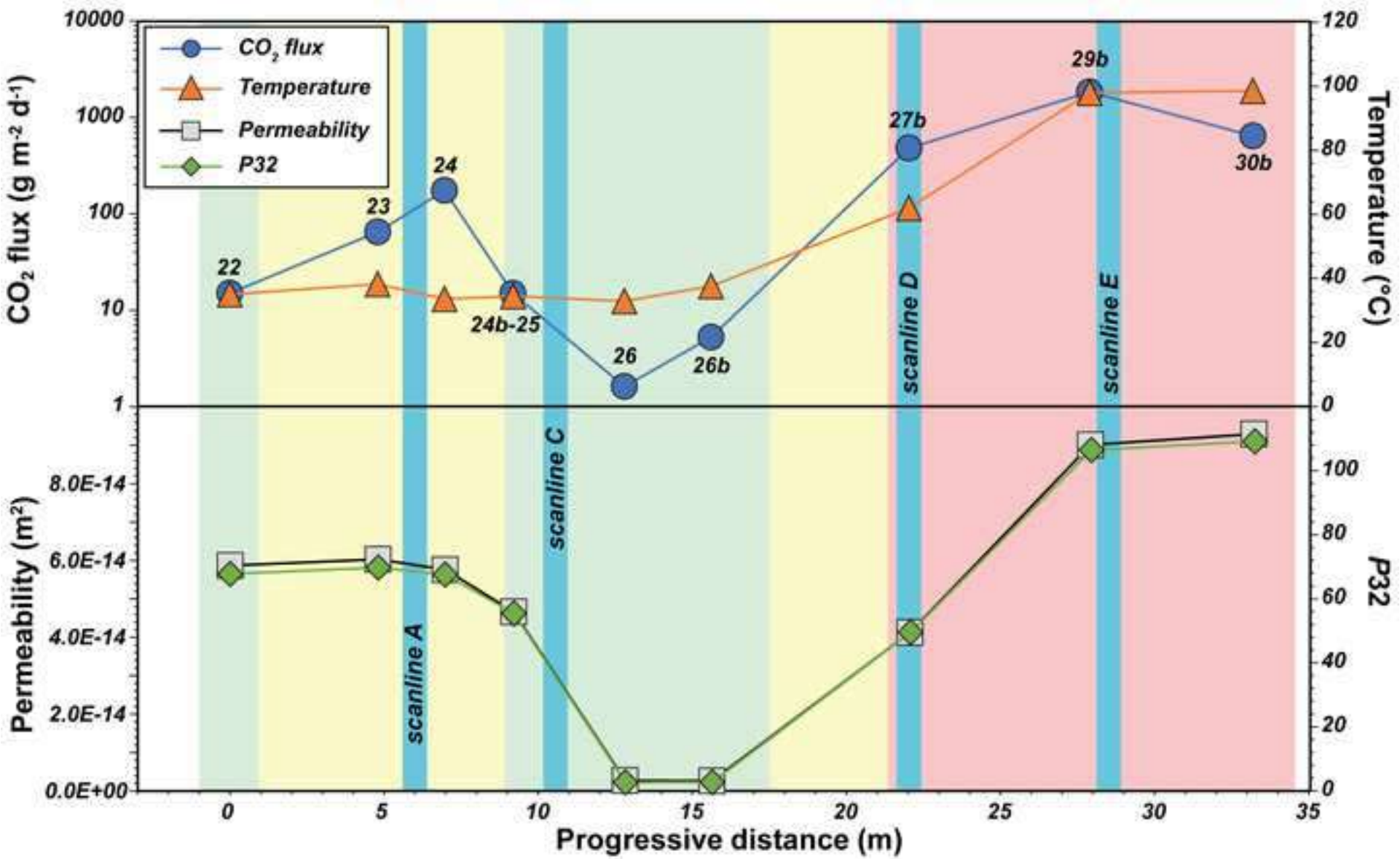

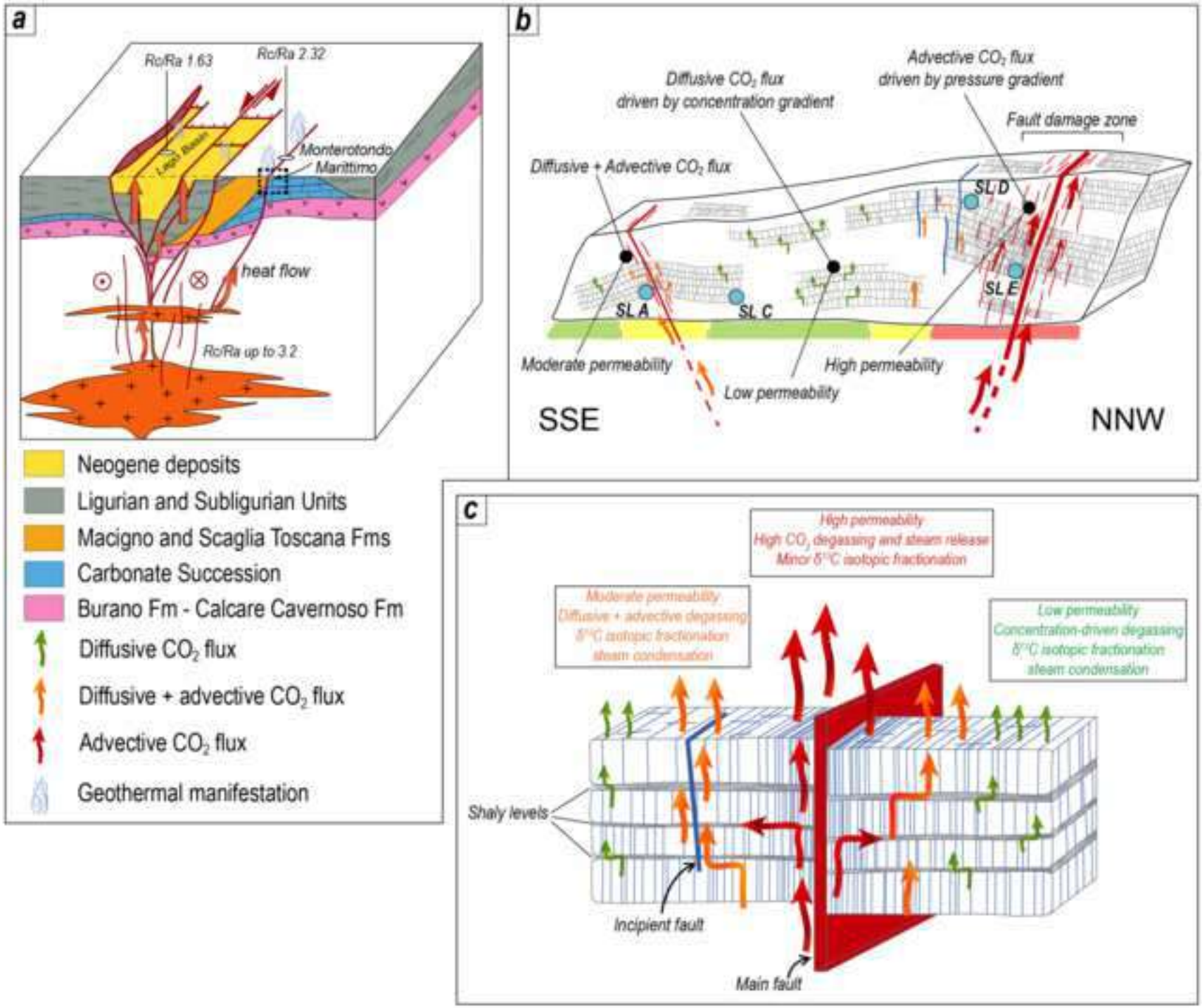

CO_2 and steam emissions by enhanced fracture permeability in the Monterotondo Marittimo-Sasso Pisano transfer fault system (Larderello Geothermal Field, Italy)

Marco Taussi [1*], Andrea Brogi [2,3], Domenico Liotta [2,3], Barbara Nisi [4], Maddalena Perrini [2], Orlando Vaselli [4,5], Miller Zambrano [6], Martina Zucchi [2]

[1] University of Urbino Carlo Bo, Department of Pure and Applied Sciences, Via Ca' Le Suore 2/4, Urbino, Italy.
[2] University of Bari Aldo Moro, Department of Earth and Geoenvironmental Sciences, Via E. Orabona 4, Bari, Italy.
[3] IGG-CNR, Institute of Geosciences and Earth Resources, Via G. Moruzzi 1 - Pisa, Italy.
[4] IGG-CNR, Institute of Geosciences and Earth Resources, Via G. La Pira 4, Firenze, Italy.
[5] University of Florence, Department of Earth Sciences, Via G. La Pira, 4, Firenze, Italy.
[6] University of Camerino, School of Science and Technology, Via Gentile III da Varano 27, Camerino, Italy

* Corresponding author: marco.taussi@uniurb.it

Declaration of interests

☒ The authors declare that they have no known competing financial interests or personal relationships that could have appeared to influence the work reported in this paper.